Available online at www.sciencedirect.com
SCIENCE DIRECT
Icarus 182 (2006) 92–117
ICARUS
www.elsevier.com/locate/icarus

Yarkovsky footprints in the Eos family

D. Vokrouhlický [a,*], M. Brož [a], A. Morbidelli [b], W.F. Bottke [c], D. Nesvorný [c], D. Lazzaro [d], A.S. Rivkin [e,1]

[a] *Institute of Astronomy, Charles University, V Holešovičkách 2, 18000 Prague 8, Czech Republic*
[b] *Observatoire de la Côte d'Azur, BP 4229, 06304 Nice Cedex 4, France*
[c] *Southwest Research Institute, 1050 Walnut St., Suite 400, Boulder, CO 80302, USA*
[d] *Observatorio Nacional, Rua Gal. Jose Cristino 77, 20921-400 Rio de Janeiro, Brazil*
[e] *Massachusetts Institute of Technology, 77 Massachusetts Av., Cambridge, MA 02139, USA*

Received 28 June 2005; revised 16 November 2005

Available online 7 February 2006

Abstract

The Eos asteroid family is the third most populous, after Themis and Koronis, and one of the largest non-random groups of asteroids in the main belt. It has been known and studied for decades, but its structure and history still presented difficulties to understand. We first revise the Eos family identification as a statistical cluster in the space of proper elements. Using the most to-date catalogue of proper elements we determine a nominal Eos family, defined by us using the hierarchical-clustering method with the cut-off velocity of 55 m/s, contains some 4400 members. This unforeseen increase in known Eos asteroids allows us to perform a much more detailed study than was possible so far. We show, in particular, that most of the previously thought peculiar features are explained within the following model: (i) collisional disruption of the parent body leads to formation of a compact family in the proper element space (with characteristic escape velocities of the observed asteroids of tens of meters per second, compatible with hydrocode simulations), and (ii) as time goes, the family dynamically evolves due to a combination of the thermal effects and planetary perturbations. This model allows us to explain sharp termination of the family at the J7/3 mean motion resonance with Jupiter, uneven distribution of family members about the J9/4 mean motion resonance with Jupiter, semimajor axis distribution of large vs small members in the family and anomalous residence of Eos members inside the high-order secular resonance z_1. Our dynamical method also allows us to estimate Eos family age to $1.3^{+0.15}_{-0.2}$ Gyr. Several formal members of the Eos family are in conflict with our model and these are suspected interlopers. We use spectroscopic observations, whose results are also reported here, and results of 5-color wide-band Sloan Digital Sky Survey photometry to prove some of them are indeed spectrally incompatible with the family.

Keywords: Asteroids, dynamics; Thermal effects

1. Introduction

The study of asteroid families has experienced a renaissance over the last several years from the discovery of several previously unknown, compact asteroid clusters (e.g., Nesvorný et al., 2002b, 2003; Nesvorný and Bottke, 2004). These discoveries can be credited, in part, to automated search programs constantly scan the sky for new near-Earth objects (e.g., Stokes et al., 2002). In the process, they have also found large numbers of main-belt asteroids, which has resulted in an unprecedented increase in the catalog of known asteroids over the last decade. These clusters are young enough that their formation ages can be directly determined by integrating their members' orbits backwards in time. Using these data, we have been able to glean new insights into space weathering processes (Jedicke et al., 2004; Nesvorný et al., 2005a), the origin of the IRAS/COBE dust bands (e.g., Dermott et al., 2001; Nesvorný et al., 2002b, 2003, 2005b), and the physics of asteroid break-up events (Nesvorný et al., 2005c).

* Corresponding author. Fax: +420 2 21 91 25 67.
E-mail address: vokrouhl@mbox.cesnet.cz (D. Vokrouhlický).
[1] Visiting Astronomer, Kitt Peak National Observatory, National Optical Astronomy Observatory, which is operated by the Association of Universities for Research in Astronomy, Inc. (AURA) under cooperative agreement with the National Science Foundation.

0019-1035/$ – see front matter
doi:10.1016/j.icarus.2005.12.011

Here, however, we focus our analysis on the Eos family, one of the largest asteroid concentrations in the main belt. This family has been studied by many groups over time; classical early references are Hirayama (1918) and Brouwer (1951), with more work in the 1970's from a variety of authors (see review in Bendjoya and Zappalà, 2002). Brouwer (1951) was the first to discover that the Eos family has some puzzling features that cannot be easily reconciled within a standard model. He noticed that the spread of family members in semimajor axis was anomalously small when compared to their proper eccentricity and inclination (see Table IV in his paper and, e.g., Zappalà et al., 1984). He hypothesized that Eos likely experienced an unusual ejection velocity field or inadequacies of the linear secular theory.[2]

Brouwer (1951) also speculated about the Eos family's age. This issue is important, because a family's age determines how long its members have been subject to post-formation dynamical evolution. Note that the chronology of asteroid families is needed to constrain collisional evolution in the main asteroid belt (e.g., Bottke et al., 2005a, 2005b). Brouwer noticed that within the simplest, linearized secular theory, the sum of proper longitude of pericenter ϖ_p and proper longitude of node Ω_p stays constant because their related proper frequencies are exactly the opposite of one another. He thus proposed to use $(\varpi_p + \Omega_p)$ as an additional parameter to test the properties of asteroid families. In particular, any strong clustering in this parameter would suggest the family is $\lesssim$1 Myr because more accurate secular theory would inevitably break this property.

An investigation of the limited number of known Eos members by Brouwer (1951, see Table V) indicated that the distribution of $(\varpi_p + \Omega_p)$ was strongly non-uniform, which could be used to argue that the Eos family is young. In spite of Carpino et al.'s (1986) finding that the $(\varpi_p + \Omega_p)$ time variation is anomalously slow in this particular zone of the main asteroid belt, Farinella et al. (1989) critically reassessed Brouwer's argument concluding it might have been fluke. By associating smaller asteroids with the Eos family, these groups showed that $(\varpi_p + \Omega_p)$ is fairly uniform, with some residual non-uniformity stemming from a potentially younger subcluster of asteroids inside the Eos family. Farinella et al. (1989) instead argued for an older age based on fact that large disruption events in the main belt occur very infrequently. They found additional support for their old age argument from the uniform rotation period distribution of the family members, which could have been produced by collisions over long time periods (Binzel, 1988). Hence, they dismissed the usefulness of the $(\varpi_p + \Omega_p)$ parameter for future family studies (except for very young families; Nesvorný et al., 2002b, 2003). We share this point of view; in Section 3.3, we show that this parameter follows a nearly uniform distribution with deviations compatible with statistical fluctuations and the expected influence of the secular resonance z_1 (compare with Milani and Knežević, 1992, 1994).

[2] As a historical curiosity, we mention that Brouwer (1951) was an opponent of the scenario that families, since their formation, had been subject to unknown perturbations, including *those of non-gravitational origin* (Brown, 1932).

Morbidelli et al. (1995) have also pointed out problems in determining the formation history and age of the Eos family. The Eos family is both bracketed by the J7/3 mean motion resonance (MMR) at ∼2.96 AU and is intersected by the J9/4 MMR at ∼3.03 AU (Fig. 2). Morbidelli et al. reported that the number of family members with $a > 3.03$ AU appears to be significantly smaller than those with $a < 3.03$ AU. It is unclear how the initial velocity distribution of fragments produced by the parent body break-up could have produced this odd arrangement. One possibility was that there was a cascade of secondary fragmentations inside the original family. No other family, however, shows any evidence for a such a process.

Morbidelli et al. (1995) also noted that 5 asteroids associated with the family were residing inside the J9/4 MMR. By numerically integrating their orbits, they found these objects are ejected from the main belt on a timescale of 100–200 Myr. Rather than postulate that these fragments were directly injected into the resonance by the family-forming event, Morbidelli et al. instead suggested that they were probably placed on those orbits via a secondary break-up. They also predicted that asteroids in the J9/4 MMR at higher (or lower) eccentricities and inclinations may also be former Eos members. Zappalà et al. (2000) confirmed this prediction when they found that 5 of the 7 objects they observed inside the J9/4 MMR (but unrelated to the family with a simple clustering method in orbital element space) had spectra compatible with Eos family members. The interesting problem with this scenario, however, is that the 5 fugitive asteroids are large enough (diameter $14 < D < 30$ km) that collisional injection over the last 100–200 Myr is highly unlikely.

Another way to estimate the age of the Eos family is to analyze the collisional evolution of its size–frequency distribution (SFD). Using a 1-D self-consistent collisional evolution code, Marzari et al. (1995) considered the SFD evolution of three prominent families: Themis, Koronis, and Eos. While partially succeeding in the Themis and Koronis cases, their match to the Eos family SFD was poor, with their best fit indicating that the Eos family was surprisingly young. It is important to note here that while Marzari et al.'s results provided us with many useful insights, their work does have important limitations: (i) the initial family SFDs were unknown, (ii) they used a disruption scaling law that allowed their asteroids to break up far more frequently than suggested by numerical hydrocodes (e.g., Benz and Asphaug, 1999), (iii) their main-belt evolution results are discordant with current constraints (Bottke et al., 2005a, 2005b), and (iv) the observed family SFDs used by Marzari et al. had not been debiased and thus were limited to $D \gtrsim 10$ km bodies.

In what follows, we show that most, though not all, of the enigmatic issues about the Eos family are naturally solved within the framework coined by Bottke et al. (2001, 2002). They argued that the asteroid families are initially more compact clusters in (a, e, i) proper element space than currently observed. The assumed ejection velocities are then compatible with numerical simulations of the asteroid catastrophic disruptions (e.g., Love and Ahrens, 1996; Ryan and Melosh, 1998; Benz and Asphaug, 1999; Michel et al., 2001, 2002), with the

observed fragments with diameters larger than few kilometers launched away at relative velocities smaller than $\simeq$100 m/s. As time proceeds, the family undergoes evolution by two processes: (i) *collisional*, with $D \lesssim 10$ km asteroids suffering catastrophic disruption within a few Gyr (and producing secondary fragments), and (ii) *dynamical*, where the thermal (Yarkovsky) forces, as a function of size, thermal parameters and rotation state (the obliquity and rotation rate, in particular; for a review see Bottke et al., 2002), spread the initial cluster in semimajor axis and allow the bodies to interact with various secular and mean motion resonances (see also Milani and Farinella, 1994, 1995; Morbidelli and Nesvorný, 1999; Farinella and Vokrouhlický, 1999; Bottke et al., 2001; Nesvorný et al., 2002a; Carruba et al., 2003, 2005; Tsiganis et al., 2003; Nesvorný and Bottke, 2004; Brož et al., 2005).

In this paper, we investigate whether the Eos family has experienced substantial evolution via the Yarkovsky effect. In Section 2, we review what we know about the Eos family (i.e., its structure in proper element space, its size–frequency distribution, the spectral properties of its members). In Section 3, we discuss anomalous family features and show, using numerical integration techniques, that they are easily understood within the Yarkovsky-dispersion model. Our model also produces some testable predictions, such as whether interloper asteroids exist inside the family. For many of these bodies, we have determined their spectra and have determined whether their spectral types are consistent with predictions (Section 4).

2. Eos family: Basic facts

In this section, we describe the known properties of the Eos family. First we applied formal clustering methods on the most updated database of asteroids to identify the Eos family in the orbital element space. Our work significantly increases the number of asteroids associated with the family as compared to previous searches (e.g., Zappalà et al., 1995; Bendjoya and Zappalà, 2002). Second, we have collected spectral information about various family members (e.g., Cellino et al., 2002, and references therein).

2.1. Identification in the proper element space

We applied the hierarchical clustering method (HCM; e.g., Bendjoya and Zappalà, 2002, and references therein) to identify clustered Eos family members in proper element space (semimajor axis a, eccentricity e and sine of inclination $\sin i$). Our database included the analytically determined proper elements of nearly 170,000 main belt numbered and multi-opposition asteroids from the AstDyS database (http://newton.dm.unipi.it/) as of November 2004. We tested different values of the cut-off velocity $30 < V_c < 85$ m/s, the principal free parameter in the HCM method. Lower values were not used to avoid the intrinsic noise of analytical proper elements.

At the largest V_c values, the cluster starts to accumulate a significant portion of the surrounding region in proper element space. This is seen in Fig. 1 where we show the number of HCM identified members of the neighboring Eos and Veritas families as a function of V_c. At the critical value $V_c = 78$ m/s, the two families coalesce into a single cluster of asteroids. This plot also demonstrates the intrinsic difficulty of family identification in case of the large families like Eos. The compact (and young; e.g., Nesvorný et al., 2003) Veritas family depends very weakly on V_c until it passes a threshold value that allows it to "join" with the background population; this means the family is distinctly defined (see also Fig. 4 of Nesvorný et al., 2005a). Conversely, as V_c is increased for Eos, the family population steadily increases as well. Not surprisingly, we expect this process to accumulate numerous interlopers. Trials and tests are needed to eliminate as many of these objects as possible from the final set.

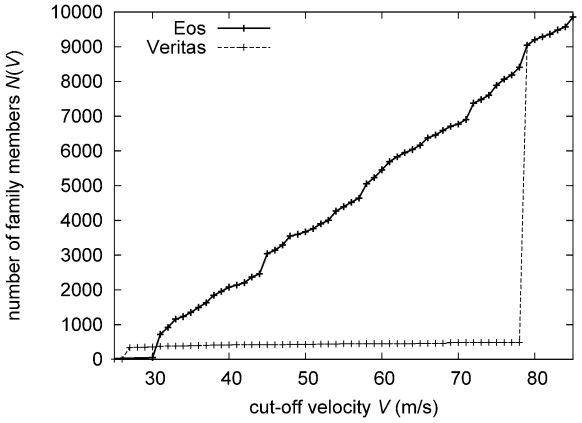

Fig. 1. Number of asteroids associated with a family (using the HCM approach) as a function of the cut-off velocity V_c for Eos (thick line) and Veritas (thin line). The large Eos family steadily accumulates asteroids as V_c increases, while identification of the compact Veritas family shows only little dependence on V_c. At a critical value of $V_c = 78$ m/s the two neighboring families coalesce into a single structure.

Fig. 2 shows two examples of Eos family identification for $V_c = 50$ m/s (left) and 55 m/s (right; dots are background main-belt asteroids inside a orbital-element box defined by the ranges of the axes). The identification of family members for different values of V_c is available at our website http://sirrah.troja.mff.cuni.cz/yarko-site/. We believe $V_c = 55$ m/s provides a reasonable compromise between completeness and overshooting; at larger V_c values, the family starts to accumulate more distant asteroids with $a > 3.03$ AU, i.e., on the far side of the J9/4 MMR with Jupiter. We use it as our nominal definition of the Eos family. Fig. 3 shows the Eos family projected onto the plane of proper a and absolute magnitude H (data are taken consistently from AstDyS website) again for two V_c values. The structure seen in this figure will be discussed in Section 3.

Note that 2-D projections of the family (Fig. 2) miss details that can be seen in 3-D proper orbital elements space. In Fig. 4 we show the Eos family as a 3-D cluster (bold symbols) embedded in the background population of asteroids (dots). We have chosen the view to emphasize the low-e and i side in order to bring attention to a stream-like structure radiating out from the family (on our website http://sirrah.troja.mff.cuni.cz/yarko-site/ we provide a computer animation that allows one to see the Eos family from many different directions in proper el-

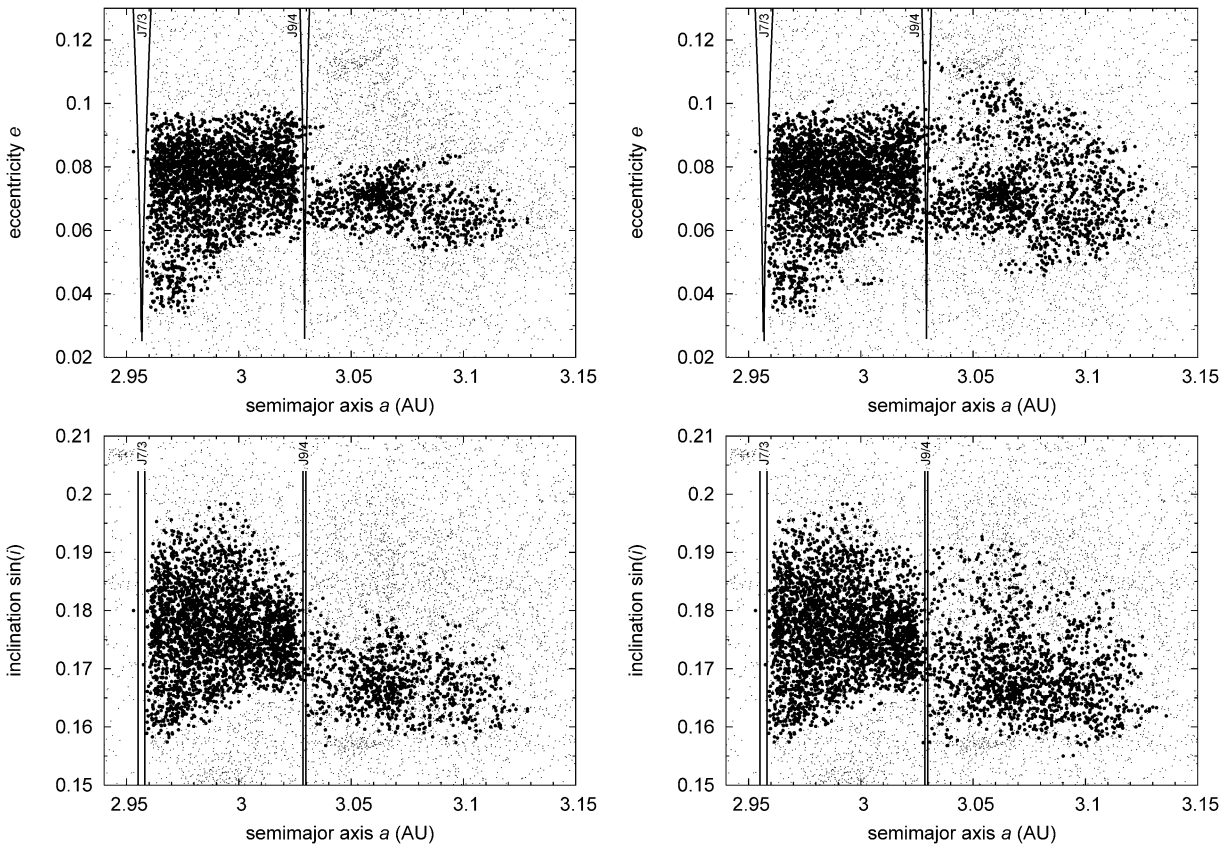

Fig. 2. The Eos family determined by the HCM with $V_c = 50$ m/s (left figures) and 55 m/s (right figures) projected onto perpendicular planes in the space of proper elements: (i) semimajor axis a and eccentricity e (upper figures), and (ii) semimajor axis a and sine of inclination $\sin i$ (bottom figures). Family members are shown by thick symbols, while the background asteroids in a surrounding box delimited by the axes range are dots. Position of major mean motion resonances with Jupiter (J7/3 and J9/4) is also shown.

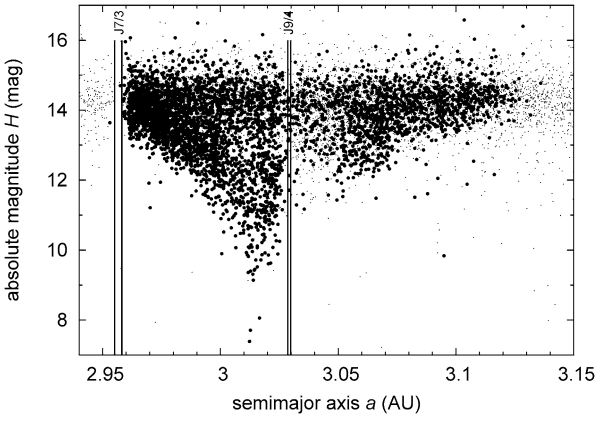

Fig. 3. The Eos family determined by the HCM with $V_c = 55$ m/s projected onto a plane of proper semimajor axis a and absolute magnitude H. As in Fig. 2, the family members are thick symbols, surrounding background asteroids are dots. Observation limits prevents detecting asteroids smaller than about 1–2 km in size ($H \simeq 17$). Major mean motion resonances are also shown.

ement space). The two planes shown in the same figure roughly mark the libration zone of the high-order secular resonance z_1 (e.g., Milani and Knežević, 1990, 1992, 1994, and Section 3.3). We see that the peculiar structure observed in the Eos family tightly adheres to this resonance (see Section 3.3 for details).

We also investigated cumulative distribution $N(< H)$ of absolute magnitudes H for Eos family asteroids. This can be achieved with high reliability, since even with low V_c values the family contains thousands of members (e.g., the nominal family with $V_c = 55$ m/s has about 4400 asteroids). Fig. 5 shows this quantity for the nominal Eos family at $V_c = 55$ m/s. We used a power-law approximation $N(< H) \propto 10^{\gamma H}$ in the magnitude range (11.5, 13.5) and obtained $\gamma \simeq 0.47 \pm 0.02$. Our value of γ is close to some previously reported values (e.g., Fujiwara, 1982) but discordant with some others who predict a considerably steeper distribution from their method (e.g., Tanga et al., 1999). This value of the power index suggests that the family has undergone significant collisional and dynamical evolution at small asteroid sizes that drove it toward the equilibrium state (e.g., Dohnanyi, 1969; O'Brien and Greenberg, 2003; Bottke et al., 2005c). In particular, Bottke et al. (2005a, 2005b) estimate a 15–20 km size asteroid (roughly $H = 11.5$ for Eos family members) has a collisional lifetime of $\simeq$2 Gyr; thus we would tentatively infer an age for the Eos family of 1–2 Gyr from this simple argument. Interestingly, our more quantitative work in Section 3.2 will provide additional support for this age.

Fig. 6 shows the best-fit power-index γ for family members with $11.5 < H < 13.5$ as a function of the cut-off velocity V_c. Except the anomalous "step" at $V_c = 44$ m/s, which is caused by a sudden extension of the family to the region beyond the J9/4 MMR (see also Fig. 1), we find that γ steadily increases. The limiting value $\simeq$0.52 can be attributed to the overall main-

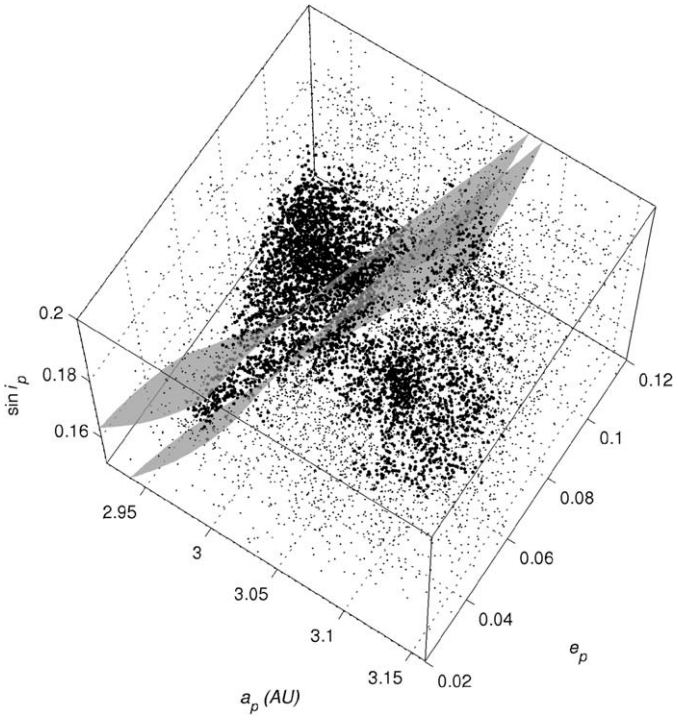

Fig. 4. The Eos family (bold symbols) shown in 3-D space of proper orbital elements; dots are background asteroids not associated with the family by the HCM method (here $V_c = 55$ m/s is used). We emphasize existence of an asteroid stream escaping from the family toward low values of the proper eccentricity and inclination. Semi-transparent surfaces indicate approximate borders of the high-order secular resonance z_1 discussed in Section 3.3. We show ± 0.8 arcsec/yr region about the exact resonance whose location is determined using a semianalytic theory of Milani and Knežević (1990, 1992); this width corresponds to the numerical results from Section 3.3. Unlike the principal MMRs, the z_1 resonance is a strongly curved 3-D structure in the space of proper elements. The observed anomalous asteroid stream and the position of the z_1 resonance strongly correlate; this suggestive link is investigated in more detail in Section 3.3.

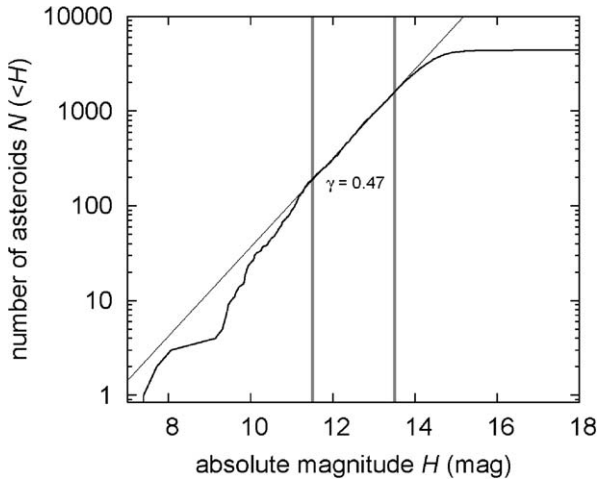

Fig. 5. Cumulative distribution $N(< H)$ of absolute magnitude values H for members of the Eos family determined by the HCM with $V_c = 55$ m/s. The straight line is a power-law approximation with index $\gamma = 0.47$ that best fits the family in the magnitude range $H \in (11.5, 13.5)$ (denoted with the two vertical lines); at larger sizes (i.e., smaller values of H) the distribution becomes steeper and dependent on individual objects, while at smaller sizes (larger values of H) the observation bias affects the data.

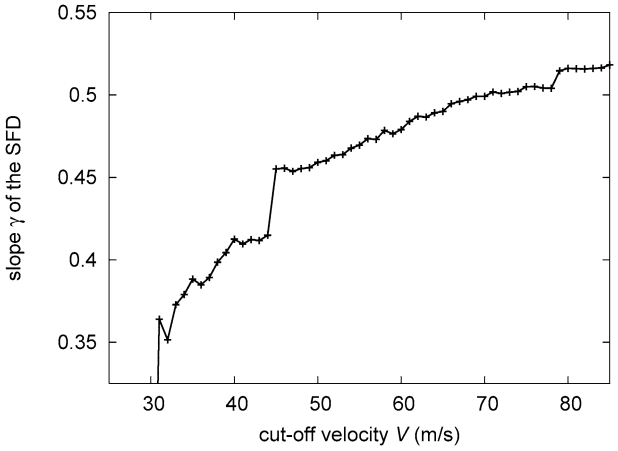

Fig. 6. The power-law index γ of the cumulative magnitude distribution $N(< H)$ fitted in the range $H \in (11.5, 13.5)$ as a function of the HCM cut-off velocity V_c. At the largest velocity the system represents basically the whole local main-belt population around the Eos family. At any smaller value of V_c the family is shallower; at our nominal family definition of $V_c = 55$ m/s we have $\gamma = 0.47 \pm 0.02$ (see Fig. 5).

belt population in this particular heliocentric zone; here V_c has become large enough to fill the entire region. The smaller γ values found for small V_c is consistent with Morbidelli et al. (2003), who predicted shallow slopes for most prominent families where their members had $H \gtrsim 15$.

2.2. Spectroscopic observations

Information about the physical properties of the Eos family members derives from spectroscopy of large asteroids, completed by numerous observers using a variety of telescopes and instruments, and broad-band photometry of small asteroids taken by the Sloan Digital Sky Survey (SDSS). Here we provide some information about both sources.

We start with results from spectroscopic surveys. Some caution is warranted when comparing data from different sources because: (i) taxonomic systems have significantly evolved over the past two decades and (ii) major surveys have only performed spectroscopy in the visible wavelengths. This later point is important because discriminating the physical properties of asteroids, especially for an object at the outskirts of the broad S-type asteroid color complex, requires additional data in the infrared. For example, Asteroid (221) Eos and several other large Eos members have visual spectra that resemble S-type objects (apart from finer details introduced only later on). It was only when an extended spectrum of (221) Eos, covering both visual and infrared bands, was obtained that Bell et al. (1987) and Bell (1989) were able to propose that Eos family members comprise a distinct spectral class now called K-type (see Veeder et al., 1995; Doressoundiram et al., 1998; Zappalà et al., 2000, for reviews of this topic).

Objects that are not related to K type are assumed to be interlopers. For example, a dedicated visual spectroscopic survey of large Eos members by Doressoundiram et al. (1998) found two asteroids, (1910) Mikkailov and (4455) Ruriko, that were spectrally similar to C-type asteroids (out of a sample of 45

observed family members). Still, there appears to be a modest spectral heterogeneity among Eos members ranging from the K types, such as (221) Eos itself, to T types (see also Xu et al., 1995). Because K and T types lie along the edge of the S-type complex, it can be difficult to precisely classify asteroids with these characteristics. Bus and Binzel (2002b), who examined 6 of the 45 asteroids discussed by Doressoundiram et al. (1998) as part of the SMASSII survey, found that 4 were K types and 2 were S types (633 Zelima and 1186 Turnera). Doressoundiram et al. (1998) interpreted the spectral differences among these bodies as some kind of weathering process or as perhaps a sign of compositional differences in the Eos parent body (see also Mothé-Diniz and Carvano, 2005). As far as we know, however, there is no general consensus about this interpretation to date.

We also note that the SMASSII survey detected 19 asteroids that are associated with the Eos family at the HCM cut-off velocity $V_c = 55$ m/s (Bus and Binzel, 2002a, 2002b; see also updates at http://smass.mit.edu). Most of them were given K-type classifications, with the exceptions being the two S-type asteroids mentioned above and two interloper asteroids classified as Xc-type asteroids: (1604) Tombaugh and (3214) Makarenko.

Another rich and recent source of spectroscopic data is the S^3OS^2 survey by Lazzaro et al. (2004) (see http://www.daf.on.br/~lazzaro/S3OS2-Pub/s3os2.htm). They observed 13 asteroids from our nominal Eos family and obtained the following results: Asteroids (1075) Helina (Xc-type), (1605) Milankovitch (X-type), (3328) Interposita (Xc-type), and (4100) Sumiko (B-type) are all spectrally diverse from prevalent K and T types in the Eos family and contribute to the interloper population. Asteroids (251) Sophia (Sl-type) and (4843) Megantic (X-type) are also recognized as interlopers. Moreover, several asteroids were re-classified as D types within the new Bus taxonomy (Bus and Binzel, 2002a, 2002b) from former T types of the Tholen taxonomy (Tholen, 1989), confirming difficulties in spectral classification.

Both datasets, SMASS and S^3OS^2, have been compiled together and applied systematically to asteroid families by Mothé-Diniz et al. (2005). For the Eos family, which was likely identified by these authors at a slightly higher V_c value, they determined that 55 out of 92 asteroids with known spectra belong to the KTD sequence; this sets the classification system for additional Eos family members. The mineralogical interpretation of these data, however, is more uncertain (e.g., D types here often have high albedo values, unlike the well interpreted low-albedo D-type objects in the outer part of the asteroid belt and among trojan asteroids). If we include Xk types in the KTD complex, which are related in the optical band, the KTD's form 74% of Eos family members. Alien, or more distant spectral types (X, C, and B) constitute 26% of asteroids in the Eos family; these values are somewhat higher than expected (Migliorini et al., 1995). Their fraction increases with larger V_c, suggesting the family is embedded in a spectrally alien zone. In spite of the ambiguous compositional implications of the KTD spectral sequence inside the Eos family, the fact that they are surrounded by primitive C-type asteroids may allow us to recognize some interlopers.

As far as broad-band photometry is concerned, we skip in this paper the older observations made for the Johnson UBV system (e.g., Zellner et al., 1985) and instead turn to more recent work of Ivezić et al. (2001, 2002), who analyzed the homogeneity of asteroid families using the broad-band 5-color data of SDSS (see http://www.astro.princeton.edu/~ivezic/sdssmoc/sdssmoc.html). Interestingly, in the case of Eos, they find a slight scatter of spectral features. Because the SDSS data are available mostly for small asteroids ($H \geqslant 12$, say), the result of Ivezić et al. might indicate spectral heterogeneity in the Eos family (e.g., Doressoundiram et al., 1998).

Nesvorný et al. (2005a) has investigated this issue using release 2.0 SDSS data. While their main focus was space weathering effects, they were able to identify SDSS colors for 457 members of the Eos family (using a larger V_c value). The average principal component values found for Eos members were $PC_1 = 0.466 \pm 0.095$ and $PC_2 = -0.104 \pm 0.083$ (standard deviations), placing this family on the outskirts of the S-complex. While that borderline position complicates interpretations, the unusual colors of some objects may help us identify them as interlopers within the Eos family (see Section 4).

Additional possible interlopers in the Eos family, suggested by the infrared broad-band photometry reported by Veeder et al. (1995), are (562) Saloma and (1723) Klemola, whose J–H color index is significantly offset from other observed members of the family. Some authors, e.g., Bell (1989), suspect the third largest asteroid associated with Eos family, (639) Latona, might be an interloper based on S-like behavior of in the infrared band.

In Section 4 we report additional spectral observations of the Eos members made over the past few years by members of our team. We also analyze the most updated SDSS data, release 3.0.

3. Eos family: Yarkovsky traces

Hereafter we analyze several outstanding features of the Eos family. We show they can best be explained within a model where the family was formed in a more compact configuration in the proper element space about 1 Gyr ago and then experienced dispersion via the Yarkovsky effects and interactions with resonances (Section 1). To that end, we performed a numerical simulation to determine how an initially compact cluster near the center of the Eos family expands in proper (a, e, i) over time. Note that our initial orbital data was chosen to be consistent with the ejection velocities predicted from laboratory experiments and numerical hydrocode simulations of asteroid disruption events (e.g., Love and Ahrens, 1996; Ryan and Melosh, 1998).

The initial orbital elements of our synthetic family asteroids were chosen according to the procedure described in the Appendix of Carruba et al. (2003). For the Eos family, the estimated mass ratio of the largest fragment and parent body is $\simeq$0.1 (e.g., Tanga et al., 1999; Campo Bagatin and Petit, 2001). Using this value, we obtain a parent body diameter of $D_{PB} \simeq 240$ km. To disrupt this object, we assumed a specific energy $Q^{\star}_D \simeq 0.1 \rho D_{PB}^{1.36}$, where the bulk density

$\rho \simeq 2.5$ g/cm^3 (Benz and Asphaug, 1999). We assume that only a small part of this energy is transformed into the kinetic energy of the dispersed fragments, such that their mean quadratic velocity $v_{\rm ej}$ is $v_{\rm ej}^2 = 2 f_{\rm KE} Q_D^\star$ (e.g., Davis et al., 1989; Petit and Farinella, 1993). The fundamental anelasticity parameter $f_{\rm KE} \simeq 0.02$ is intentionally chosen small, such that $v_{\rm ej}$ is on the order of a few tens of meters per second.

Following the work of Petit and Farinella (1993), we also adjust our velocities to account for the self-gravity of the parent body, such that the escaping fragments must have a positive binding energy value. We also assumed $v_{\rm ej}$ had a Maxwellian distribution. For simplicity, no mass/size dependence of $v_{\rm ej}$ was assumed. The initial velocity field was set to be isotropic in space, although below we shall argue that the properties of the family indicate this may be an unrealistic assumption. Finally, we transformed the initial velocity field into orbital elements using Gauss equations and estimates of the parent body's true anomaly f and argument of pericenter ω: $f = 90°$ and $\omega + f = 45°$ (see, e.g., Morbidelli et al., 1995). This latter choice is somewhat arbitrary, but it produces an initial family which has a characteristic, but not extreme, extent in the proper element space for the given ejection velocities.

We use a SWIFT-RMVS3 integrator (e.g., Levison and Duncan, 1994) modified to account for the Yarkovsky forces (see http://sirrah.troja.mff.cuni.cz/yarko-site/ for details of its implementation, speed and accuracy tests). We also complemented the original version of the integrator with computations of synthetic proper elements in a manner compatible with definition laid out in Knežević and Milani (2000, 2003). This means that we first apply a Fourier filter to the (non-singular) orbital elements in a moving window of $\simeq$0.7 Myr (with steps of 0.1 Myr) to eliminate all periods smaller than some threshold (1.5 kyr in our case; we use a standard sequence of Kaiser windows as in Quinn et al. (1991), a procedure equivalent to what is used by Knežević and Milani, 2000). The filtered signal, mean orbital elements, is then output from the simulation for further checks and passed through a frequency analysis code adapted from Šidlichovský and Nesvorný (1997) to obtain (planetary) forced and free terms in Fourier representation of the orbital elements. The isolated free terms are what we use as the proper orbital elements.

The 4 jovian planets are included in our simulation with their masses, initial positions and velocities taken from the JPL DE405 ephemeris. The effect of the terrestrial planets are accounted for as a barycentric correction of the initial conditions only, which we believe is justified in this distant zone of the asteroid belt. A timestep of 20 days is used. We used 210 test particles (asteroids) in our runs. Their diameters range from $D = 2$ to 60 km. Smaller bodies dominate our integrated sample such that we have 10 bodies with $D = 60$ km in our sample and there are $\propto 1/D$ bodies in different size bins.

Their rotation rate distribution is set to be a Maxwellian with a peak value corresponding to a period of 8 h (though we prevent shorter/longer periods than 4/12 h; e.g., Binzel, 1988). The orientation of their spin axes is assumed to be uniform in space.[3] The rotation parameters of the asteroids are assumed to be constant for these runs. We acknowledge this is an over-simplification; thermal and gravitational torques produce large variations of asteroid spin vectors on Gyr timescales (see, e.g., Section 3.2). Here, however, we trade complexity for simplicity. The thermal parameters of the asteroids, necessary for modeling Yarkovsky forces, are: thermal conductivity $K = 0.005$ W/m/K, specific heat capacity $C_{\rm p} = 680$ J/kg/K, and surface/bulk densities 1.5 and 2.5 g/cm^3, respectively. We assume that multi-kilometer asteroids in the Eos region have an insulating surface layer of dust or at least a significant porosity which makes K small. We use analytic formulae from Vokrouhlický (1998, 1999) and Vokrouhlický and Farinella (1999, Appendix) to compute the diurnal and seasonal variants of the Yarkovsky effect. With our chosen thermal parameters, the diurnal effect is about an order of magnitude larger than the seasonal effect, allowing asteroids with retrograde spins to spiral toward the Sun and those with prograde rotations to spiral away from the Sun.

After setting the initial conditions and thermal parameters for our test asteroids, we let our synthetic family evolve for 1 Gyr (this end-time was chosen to be in rough accordance with our estimate of the family age in Section 3.2). Figs. 7 and 8 show the dynamical evolution of their proper (a, e, i) over time (solid lines), superimposed onto positions of the currently observed Eos family members (dots). The former figure tracks evolution of asteroids with size $D \geqslant 7$ km, while the latter is for asteroids with $D \leqslant 7$ km. In both figures, we show the position of major MMRs—J7/3, J9/4, and J11/5—as well as numerous weaker MMRs such as high-order resonances (e.g., J16/7 or J23/10) and three-body resonances with Jupiter and Saturn (e.g., 8J–3S–3, 6J+2S–1, 5J–1S–2, or 3J–2S–1[4]; Nesvorný and Morbidelli, 1998; Morbidelli and Nesvorný, 1999; Morbidelli, 2002).

The effect of resonances on orbits migrating in a is twofold, depending of the strength of the resonance and the drift rate $({\rm d}a/{\rm d}t)$. Weak resonances can temporarily capture an orbit and change its proper e and/or i by a small amount upon leaving the resonance (Fig. 9; see also Bottke et al., 2000; Vokrouhlický and Brož, 2002). This effect, while small enough to keep asteroids in the family, increases the mean dispersion of e and i over time. Our simulations suggest that this effect allows our test asteroids to match the full extent of the observed family in e but not in i, where it misses about a factor of two. Our integrations, however, assume fixed orientation of the spin axis in space for our test asteroids; in reality, thermal and gravitational torques, together with collisional effects, may produce more complicated evolutionary paths. For example, ${\rm d}a/{\rm d}t$ can change, or even reverse sign, in time in response to spin axis

[3] A semi-empirical model of Paolicchi et al. (1996) suggests a size–rotation relation with smaller fragments rotating faster than the large ones. Given other uncertainties in our simulation, we stay with our simple formulation.

[4] We adopt the notation of Nesvorný and Morbidelli (1998) and Morbidelli (2002) who characterize a three-body MMR $(+m_{\rm J}{\rm J} + m_{\rm S}{\rm S} + m)$ with a condition $m_{\rm J}\dot\lambda_{\rm J} + m_{\rm S}\dot\lambda_{\rm S} + m\dot\lambda \simeq 0$, where $\lambda_{\rm J}$, $\lambda_{\rm S}$, and λ are mean longitudes of Jupiter, Saturn, and the asteroid.

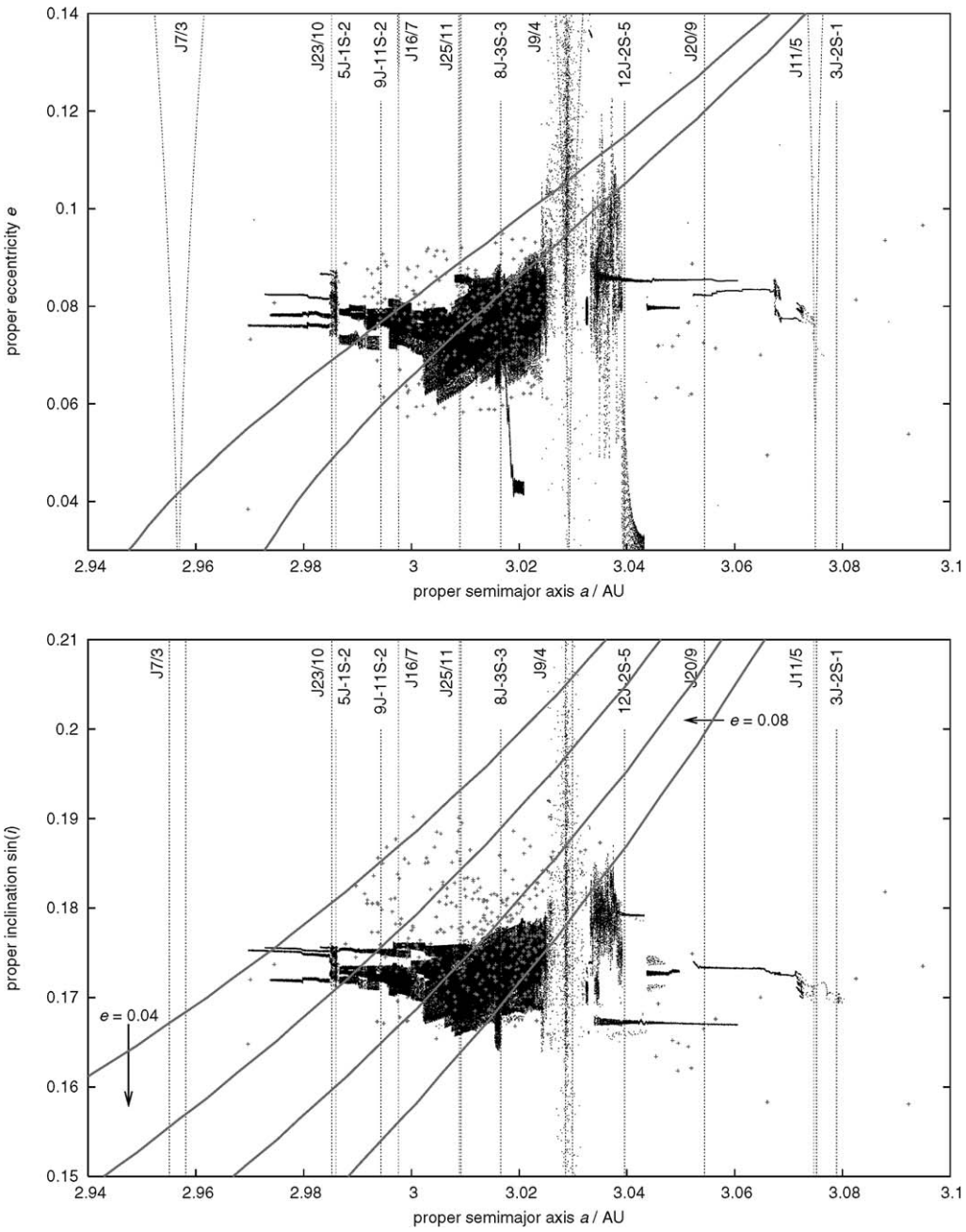

Fig. 7. Evolution tracks of our synthetic Eos asteroids with size $\geqslant$7 km during 1 Gyr in our simulation; dots are $\geqslant$7 km members of the currently observed family with the HCM threshold velocity $V_c = 55$ m/s. Top: proper eccentricity vs proper semimajor axis; bottom: proper sine of inclination vs proper semimajor axis. The initially compact family extends in course of time due to a combination of the (i) Yarkovsky forces that produce diffusion in the semimajor axis, and (ii) interaction with MMRs that, upon capture, cause eccentricity and inclination to change. The latter effect is proportional to the resonance strength scaling with its order. Thus the principal resonances—here J9/4—make many of the captured asteroids eliminated from the family. Weaker MMRs, such as 16/7 or the three body resonances (shown in the figure), do not have a capability to eliminate asteroids from the family, yet they can make the family to extend in eccentricity and inclination. A special effect is produced by the high-order secular z_1 resonance (Section 3.3) that make the Yarkovsky-drifting orbits frequently captured and driven along it for a long period of time. This is because this resonance varies along all proper elements, approximately diagonally across the family. The gray curves show nominal location of the resonance ± 0.8 arcsec/yr zone for: (i) $\sin i = 0.17$ (top), and (ii) $e = 0.04$ and $e = 0.08$ (bottom). The particle moving toward small proper eccentricity value at $\sim$3.02 AU shows a rare temporarily capture in a weak secular resonance $g - 3g_6 + 2g_7$.

evolution, allowing them to cross back and forth across weak resonances at variable speeds. This could help increase their dispersal in e and i. It is also possible that our initial velocity field was unrealistic; perhaps a more accurate velocity field would help eliminate the "inclination problem" (Section 5). We note, however, that effect of dispersion in e and i is size-dependent since smaller asteroids have chance to meet more tiny resonances as they migrate faster than large asteroids. This effect helps explaining "triangular" shape of the families in the e–H and i–H planes discussed by Cellino et al. (2002).

Powerful MMRs, namely the J7/3, J9/4, and even the J11/5, can remove Eos asteroids from the family by significantly in-

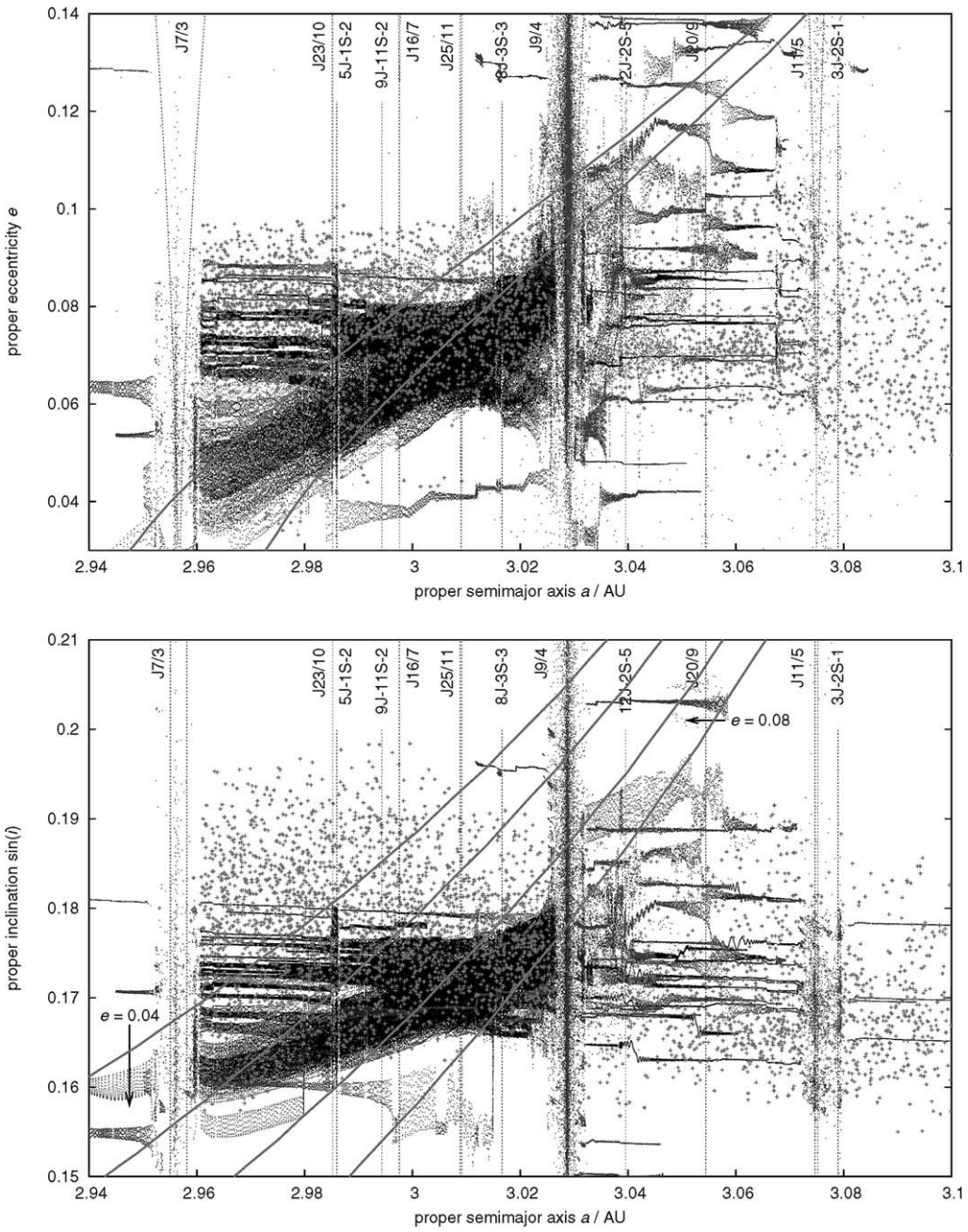

Fig. 8. The same as in Fig. 7 but here for asteroids with size $\leqslant 7$ km (view dominated by 2-km-size bodies). These objects have a faster semimajor axis drift due to the Yarkovsky forces and some manage to cross the whole extend of the family in semimajor axis. As in Fig. 7 we note both interaction with the weak MMRs and significant role of the z_1 secular by trapping the migrating objects and transporting them to smaller values of proper inclination and eccentricity. With that process, nearly the complete eccentricity extend of the family is achieved, though effect on inclination is still small. Transparency of the J9/4 MMR for the migrating objects is higher now, yet many asteroids still get ejected from the Eos family via this route. The J7/3 MMR may eventually be also crossed by few of these smaller asteroids, but upon this crossing the eccentricity and inclination get largely changed. The black sections of the evolutionary tracks indicate the particle is still associated with the Eos family at the nominal HCM cut-off velocity $V_c = 55$ m/s; the dark-gray section indicate the particle escaped too far from the family and ceases to be associated with it. Note, that the few objects that crossed the J7/3 resonance became unrelated to the Eos family at the adopted nominal HCM cut-off velocity.

creasing (or decreasing) their e and/or i values. The strength of this effect is proportional to the order of the resonance (e.g., Morbidelli, 2002), but it also depends on the Yarkovsky $\mathrm{d}a/\mathrm{d}t$ rate. In the Eos family, we have a wide range of possible outcomes, from the near total elimination of observable asteroids (J7/3 MMR) to their partial elimination (J9/4 MMR). Both produce quantitatively testable effects: termination of the family in the former case and a rate-dependent drop in the semimajor axis density of asteroids after passage of the latter. We devote Section 3.1 to a careful study of this effect.

Fig. 10 shows a close up of asteroids drifting into the J11/5 and 3J–2S–1 resonances. This doublet may cause the partial elimination of bodies from the family, mainly because the bodies reaching this resonance may have had their eccentricities

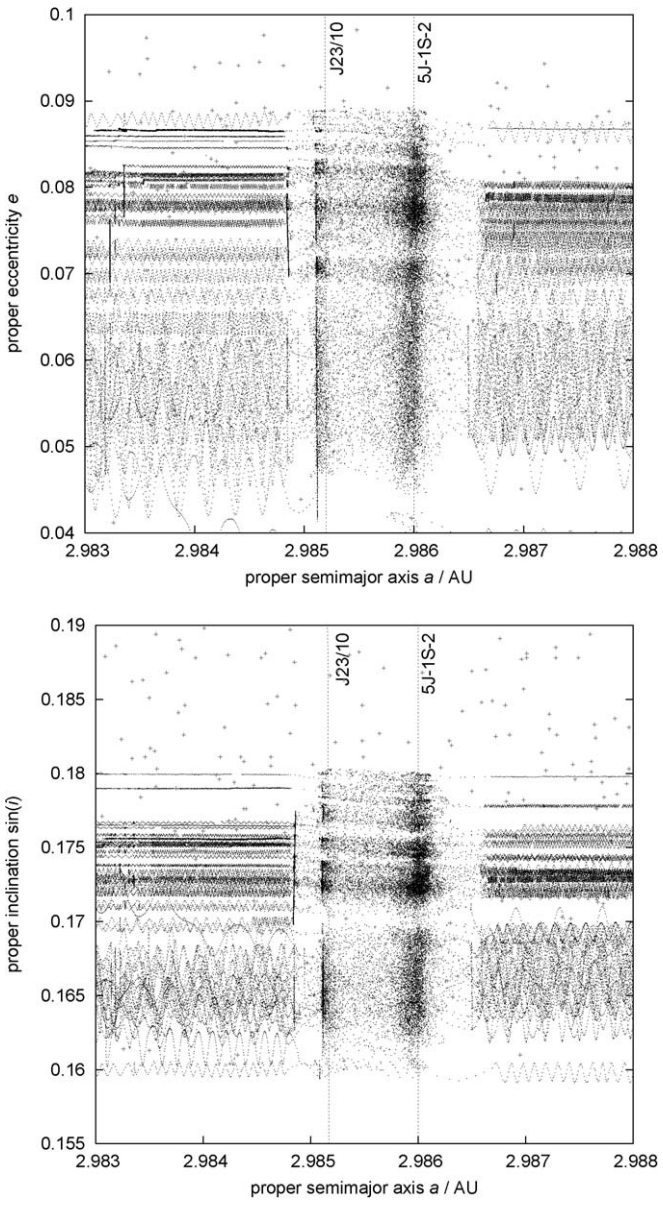

Fig. 9. A zoom of Fig. 7 showing tracks of particles in our simulation near a pair of weak mean motion resonances J23/10 and 5J–1S–2 (see the text for nomenclature); dots are the currently observed asteroids. Upper panel is a projection onto the proper eccentricity vs proper semimajor axis values, lower panel gives a projection onto the proper sine of inclination vs proper semimajor axis values. Because of the Yarkovsky forces the orbits migrate toward smaller semimajor axis values. Upon encounter the mean motion resonances, the proper eccentricity might be significantly changed; the inclination effect is quite less for these resonances. The bottommost migrating particles are trapped in the z_1 secular resonance and stay so even after a period of interaction with the mean motion resonances.

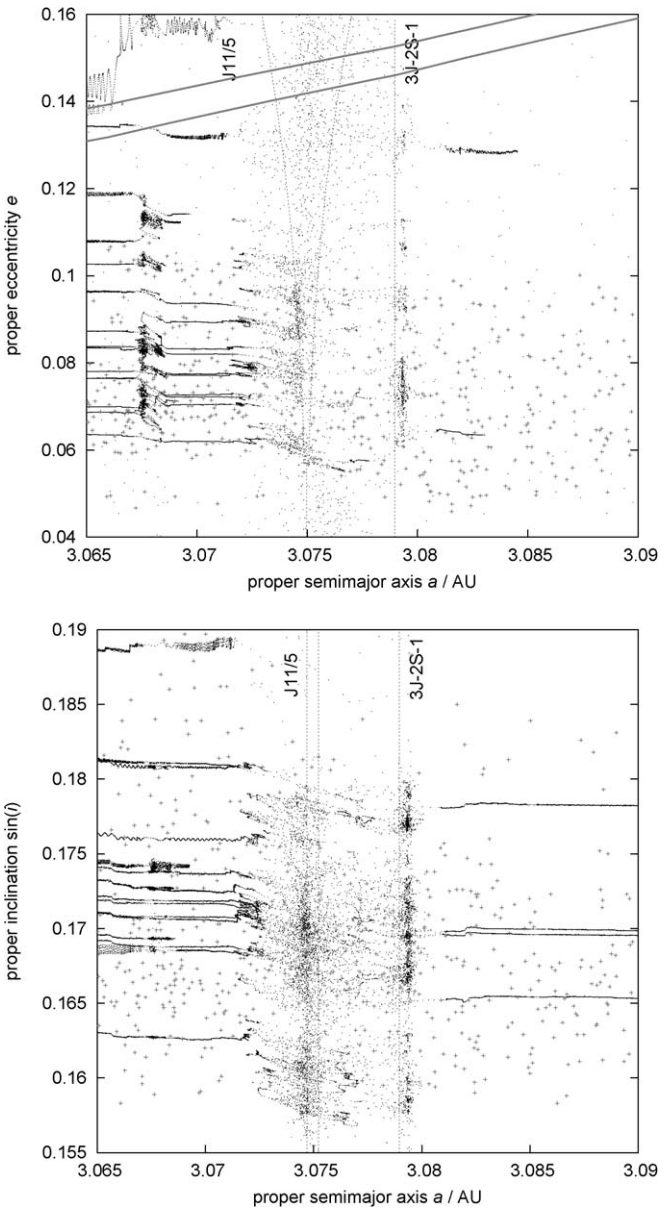

Fig. 10. A zoom of the evolutionary paths of the Eos members in our simulation near the J11/5 and 3J–2S–1 resonances. This doublet causes a non-negligible elimination rate and only orbits at sufficiently low initial e value have a good chance to continue populating the family at $a \geqslant 3.08$ AU.

"pumped up" by a previous interaction with the J9/4 resonance. The probability of crossing this doublet is higher at low eccentricity. For example, Fig. 2 shows the family at $V_c = 55$ m/s first extends beyond the J11/5 and 3J–2S–1 resonances at e values.

The last resonant effect, very specific to the Eos family, is the influence of the high-order secular resonance z_1 (e.g., Milani and Knežević, 1990, 1992, 1994). While it will be described it more detail in Section 3.3, we note that many asteroids in our simulation adhere to this resonance and follow a "diagonal route" toward smaller values of proper e and i. At the same time, their location in this resonance makes their proper e and i values oscillate with large amplitudes and a period of several Myr. Asteroids migrating toward large a values can also follow this secular resonance, but they are frequently blocked and removed from the family by the J9/4 MMR.

Using these simulations to set the stage for our work, we are now ready to discuss some of the more interesting features of the Eos family in greater detail.

3.1. J7/3 and J9/4 MMR tests

The fact that the Eos family is terminated by the J7/3 MMR (Figs. 2 and 3) is one of its most important and interesting prop-

erties. Examples of other prominent families terminated by resonances include the Koronis family (terminated by the J5/2 and J7/3 MMRs; Bottke et al., 2001) and Eunomia families (terminated by the J3/1 MMR; Morbidelli and Vokrouhlický, 2003). We note that the width of J7/3 MMR, at the mean eccentricity value of the Eos orbits, is $(\Delta a)_{7/3} \simeq 7 \times 10^{-3}$ AU. This value can be approximately interpreted in terms of a HCM velocity distance $(\Delta v)_{7/3}$ as $(\Delta a)_{7/3}/a_{7/3} \simeq (\Delta v)_{7/3}/v_{7/3}$; here $a_{7/3}$ is the position of the resonance and $v_{7/3}$ is the characteristic orbital velocity at the resonance. With this relation (that assumes no difference in eccentricity and inclination), we estimate the J7/3 MMR presents an "obstacle" of $(\Delta v)_{7/3} \simeq 10$ m/s in the HCM scheme. This estimate was obtained using the circular three-body problem. The true width of the J7/3 MMR might be little larger, but using $V_c = 55$ m/s should allow us to pick up any missing components of the Eos family that happen to reside beyond the J7/3 MMR. Even at $V_c = 70$ m/s, however, very few asteroids are found, and these objects most likely represent the background population.

We thus conclude that the Eos family does not extend beyond the J7/3 MMR, even though it tightly adheres to it along a significant range of e and i values. This configuration is inconsistent with its emplacement from the initial velocity field (e.g., Zappalà et al., 1996; Cellino et al., 1999). Instead, we conclude the initial family dynamically evolved to meet the J7/3 MMR border over time via the Yarkovsky effect. Asteroids reaching the resonance were presumably eliminated by becoming trapped in the resonance and then having their e values pumped up to planet-crossing values (Bottke et al., 2001).

To verify our claim, we placed 102 test asteroids of a given size along the outside border of the J7/3 MMR ($a > 2.96$ AU) and then used numerical integration to track the evolution of these bodies into the resonance by the Yarkovsky effect. As initial data, we used the osculating orbital elements of real Eos members located close to the J7/3 MMR. the obliquities of the objects were set to 135° for each test asteroid. The thermal parameters and rotation rates were chosen to be the same as in the numerical simulation described above. We investigated five characteristic sizes corresponding to the absolute magnitudes $H = 13$, 14, 15, and 16 (we use the mean albedo $p_V = 0.13$ for the size–magnitude conversion). Note that $H = 13$ is the approximate limiting value at which the family members adhere to the J7/3 MMR (see Fig. 3). We also note that $H = 13$–14 is about a current completeness limit at the location of the Eos family (Jedicke, R., personal communication). The observation incompleteness beyond this limit is, however, uncorrelated with processes we study below and thus should not affect our conclusions.

Table 1 summarizes the results of our experiment. In general, only the smallest asteroids with low e and i crossed the J7/3 MMR. For $H = 16$ bodies ($D \simeq 2.4$ km), we recorded 13 such cases (out of 102). We conclude that (i) most Eos family members cannot cross this resonance and (ii) a few kilometer-sized asteroids with $a < 2.96$ AU might be Eos escapees. These putative objects would originate from the low e, i tail of the Eos family that is not densely populated (see below for explanation); most family members have $e \geqslant 0.07$. Finally, we point out that $H > 16$ bodies are hard to detect with current survey capabilities and the first populated magnitude bin is centered about $H = 15$ with lower crossing probability.

Table 1
Statistics of Yarkovsky-drifting orbits crossing the J7/3 MMR

H (mag)	D (km)	N	N_c
13	9.4	102	0
14	5.9	102	6
15	3.7	102	7
16	2.4	102	13

Note. H and D are the absolute magnitude and size of the particles (assuming $p_V = 0.13$), N is the number of integrated orbits, N_c is the number of orbits that crossed the J7/3 MMR without being scattered enough in the inclination and eccentricity to remain approximately in the appropriate range of Eos members.

Table 2
Statistics of Yarkovsky-drifting orbits crossing the J9/4 MMR

H (mag)	D (km)	N	N_c
10	37.4	102	2
11	23.6	106	6
12	14.9	102	12
13	9.4	106	15
14	5.9	106	21
15	3.7	106	30
16	2.4	106	35

Note. The first three columns as in Table 1 except here for the J9/4 MMR; N_c is the number of particles that were still associated with the nominal Eos family after the passage through J9/4 MMR during their further evolution.

The case of the J9/4 MMR is even more interesting than the J7/3 MMR because it allows us to quantitatively test our Yarkovsky-drift model. This is because the J9/4 MMR is weak enough that many observable asteroid can jump the resonance (Bottke et al., 2000). On the other hand, the J9/4 MMR is powerful enough to trap and eliminate some fraction of asteroids trying to cross it. Thus, the J9/4 MMR is analogous to a river with a strong current; weak swimmers are swept downstream while strong swimmers can reach the opposite bank.

The ratio of eliminated/crossing test asteroids for a given size can be compared to observations of Eos family members on both sides of the J9/4 MMR. To make this comparison, we again integrated a large number of test asteroids and let them drift into the J9/4 MMR. Here we chose the osculating orbital elements of 106 real Eos members with proper $a \in (3.023, 3.027)$ AU and gave them $H = 10$–16. The obliquity was set to 45°, allowing the asteroids to drift outward to encounter the J9/4 MMR.

Table 2 gives our results. As expected, significantly more asteroids, as compared to the J7/3 case, crossed this higher-order resonance. To compare this data with observations, however, we need to make additional assumptions. This is because of two reasons. First, the J9/4 MMR is miscentered in the family, for its position at $a_{9/4} \simeq 3.03$ AU is to be compared with the family center at $a_c \simeq 3.02$ AU. Thus, there is a priori bias to have more Eos members below the J9/4 than above and we have to correct for this effect. Second, the left side of the family is cut

by the J7/3 resonance. As a result, distribution of asteroids with $a \leqslant a_c$ gives us only a limited information not extending below $a_{7/3} \simeq 2.957$ AU. Our procedure is as follows.

We first concentrate on the Eos region that corresponds to $a \leqslant a_c$, where the family's center $a_c \simeq 3.02$ AU. We denote the density distribution of members with a given H by $\mathcal{B}(a; H)$. Thus

$$\mathcal{B}(a; H) = \frac{\mathrm{d}N}{\mathrm{d}a}, \tag{1}$$

where $\mathrm{d}N$ is number of Eos members in the semimajor axis interval $(a, a+\mathrm{d}a)$ with $a \leqslant a_c$ and having an absolute magnitude near H. Assuming that the initial distribution of Eos members is symmetric about a_c, we expect

$$N^{<}_{\mathrm{exp}}(H) = \int_{a_{7/3}}^{a_{9/4}} \mathcal{B}(a; H)\,\mathrm{d}a \tag{2}$$

asteroids of absolute magnitude H to reside in the Eos family on the left-hand side of J9/4 MMR, thus with $a_{7/3} < a < a_{9/4}$, where $a_{7/3} \simeq 2.9757$ AU and $a_{9/4} \simeq 3.03$ AU. We also define

$$N^{>}_{\mathrm{exp}}(H) = \int_{a_{9/4}}^{2a_c - a_{7/3}} \mathcal{B}(a; H)\,\mathrm{d}a \tag{3}$$

as the number of asteroids with a given H to reside in the Eos family with $a > a_{9/4}$ (we also assume here $\mathcal{B}(a; H) = \mathcal{B}(2a_c - a; H)$ which expresses symmetry of the $\mathcal{B}$-function about a_c). Denoting $N^{<}_{\mathrm{obs}}(H)$ and $N^{>}_{\mathrm{obs}}(H)$ the numbers of truly observed family members on either size of the J9/4 MMR, and with semimajor axis value specified by limits in Eqs. (2) and (3), we finally define

$$r(H) = \frac{N^{>}_{\mathrm{obs}}(H)/N^{>}_{\mathrm{exp}}(H)}{N^{<}_{\mathrm{obs}}(H)/N^{<}_{\mathrm{exp}}(H)}. \tag{4}$$

The value of $r(H)$ is a measure of how the true Eos population disperses/evolves toward smaller/larger a values. In particular, if $r \simeq 1$, the family dispersion is equal on both sides of J9/4 MMR.

Fig. 11 shows the ratio $r(H)$ for the Eos family identified with three HCM velocity cut-offs: 50, 55 (nominal value; thin line), and 60 m/s. The fact that $r(H)$ is always smaller then unity quantitatively confirms that there is a net depletion of the observed members in the Eos family on the right side of the J9/4 MMR. We also note, that $r(H)$ is strongly size-dependent, such that there is a paucity of large family members beyond the J9/4 MMR with $a > a_{9/4}$.

This observation is inconsistent with a static model where Eos family members remain in the same orbits (see the discussion in Morbidelli et al., 1995). In our scenario, however, the $r(H)$ values are a natural outcome of Yarkovsky evolution, with larger Eos members eliminated as they try to cross the resonance. In fact, if we had an ideal model, the $r(H)$ values should equal the probability that our integrated test asteroids cross the J9/4 MMR ($c(H)$) (Table 2). For his reason, Fig. 11 shows the crossing probability $c(H)$ together with $r(H)$.

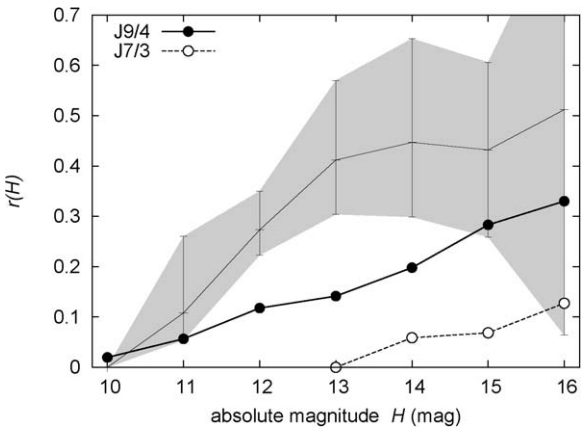

Fig. 11. The thin line shows ratio $r(H)$, from Eq. (4), of the observed vs expected Eos members on the right over left-hand sides of the J9/4 MMR as a function of the absolute magnitude H; we consider bodies binned in 0.5 zones of H about $H = 10$–16 with the last value, however, having large uncertainty due to few known objects only (see Fig. 3). The shaded uncertainty interval is based on computed $r(H)$ values for Eos family identifications with V_c in the range 50–60 m/s (lower values for smaller V_c). Values $r < 1$ indicate a relative paucity of Eos members above the J9/4 MMR as regards to the population below the J9/4 MMR. The solid line shows probability to cross the J9/4 MMR for orbits migrating toward larger semimajor axis values by the Yarkovsky forces (symbols are data in Table 2). The lowest dashed line is the same for the J7/3 MMR.

Overall, we find a rough agreement between $r(H)$ and $c(H)$. In particular, both indicate very few bodies with $H \leqslant 10$ should be able to cross the J9/4 MMR. The principal difference is in the crossing probabilities for $H = 12$–14 asteroids, where $r(H) > c(H)$. We find several possible reasons for this mismatch:

- For $r(H)$ to match $c(H)$, all asteroids must cross the resonance. Our model in Section 3.2, however, indicates that some asteroids might be initially thrown to orbits with $a > a_{9/4}$. If true, we need to modify our model assumptions. The best-fit solution from Section 3.2 predicts this happens for $H \geqslant 13$ and it may help increasing the local population of the Eos members with $a \geqslant a_{9/4}$.
- Asteroids below some size threshold might reach the J9/4 MMR with smaller obliquity values and thus would migrate faster than the model asteroids in our simulation. Such a result might be produced by the YORP effect, which would have perhaps 1 Gyr to work (Section 3.2). The work of Vokrouhlický et al. (2003), and previous theoretical studies, suggest $D \simeq$ (30–40) km Koronis asteroids complete the YORP cycle (i.e., approach an asymptotic obliquity value) in ∼2.5 Gyr. Scaling from this result, and using the mean albedo value $p_V \simeq 0.13$ for Eos family members, we estimate that $H \geqslant 12$ asteroids are small enough ($D \leqslant 15$ km) to reach near asymptotic YORP obliquity states within 1 Gyr. This would efficiently shift data points corresponding to $H \geqslant 12$ in Fig. 11 by -0.75 while helping bring $c(H)$ and $r(H)$ closer together.

Thus, while model and observation are not in perfect agreement, we consider the results of our test satisfactory.

3.2. *a–H projection analysis*

Like other families, the Eos family shows an inverted triangular pattern when its members are projected onto the plane defined by a and H: the largest asteroid resides near the mean value of a for the family, while extreme values of a are occupied by small asteroids (Fig. 3). Because it appears natural that smaller fragments received larger relative velocities with respect to the parent body during the initial ejection phase, Cellino et al. (1999) attempted to use this distribution to calibrate the unknown size–velocity distribution for the fragments. It turns out, however, that a significant portion, though not 100%, of this plot is produced by Yarkovsky evolution (Bottke et al., 2001, and below). Thus, we can only reconstruct the initial size–velocity distribution by first accounting for evolutionary processes.

As we will describe below, we used the methods described in Vokrouhlický et al. (2005) to determine the initial velocity distribution of the Eos family. Our results indicate that ejection velocities gave the Eos family an extension in a equivalent to ∼30–50% of the spread of the observed family. The remainder was produced by Yarkovsky drift/dynamical dispersion produced by resonances. These results are in good agreement with an independent analysis of Dell'Oro et al. (2004), who suggest that the initial families were statistically smaller than the observed families by a factor of two. Our work is quantitative enough to allow us to estimate the age of the Eos family, and it complements and improves upon the results described in Nesvorný et al. (2005a).

3.2.1. *Method*

Here we briefly describe the method of Vokrouhlický et al. (2005) used to analyze the semimajor axis dispersion on an asteroid family. Consider family members plotted in the 2-D space (a, H). In order to transform this data into a 1-D space, Vokrouhlický et al. (2005) introduced the parametric relation

$$0.2H = \log(\Delta a/C) \tag{5}$$

between H and Δa. Here $\Delta a = a - a_c$, where a_c is the center of the family and C is a free parameter that can be positive or negative. The family can then be characterized by a distribution of C values. We define the distribution function as

$$\mathcal{D}(C) = \frac{\mathrm{d}N}{\mathrm{d}C}, \tag{6}$$

where $\mathrm{d}N$ is the number of family asteroids in a strip of (a, H) generated by changing C in the range $(C, C + \mathrm{d}C)$. This approach allows the function $\mathcal{D}(C)$ to contain all of the family's data. We can then test various family configuration models in (a, H) space by comparing them with the observed $\mathcal{D}(C)$ distribution (using a pseudo-χ^2 methods).

The choice of the template function (5), and the related distribution (6), instead of the simple distribution $\mathcal{B}(a; H)$ of semimajor axis values has been motivated by simple models involving purely either Yarkovsky dispersion or fragment ejection with velocity strictly inversely proportional to their size. Both would yield $\mathcal{D}(C)$ constant. So any deviation from a uniform $\mathcal{D}(C)$ distribution could be translated into a deviation from these "toy models." Luckily, these go in a rather opposite way. A static model, with no dynamical evolution of the family, but velocity field either anisotropic and/or with a velocity dispersion for fragments of a given size, give typically $\mathcal{D}(C)$ concentrated near the origin or with a single maximum, asymmetric to the origin. Conversely, the model where combined Yarkovsky and YORP dynamical evolution of the family plays an important role results in $\mathcal{D}(C)$ that has two maximum values symmetrically offset from the origin $C = 0$.

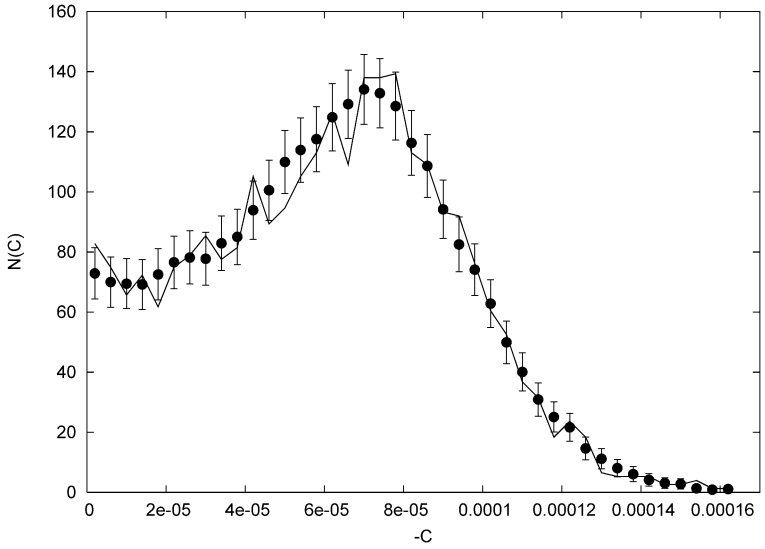

Fig. 12. Comparison of the observed and modeled distribution $\mathcal{D}(C)$ for the Eos family; here we use model with size-independent velocity V_{SD} that characterizes dispersal of the initial fragments along all directions. We actually show directly number $N_{obs}(C)$, and $N(C)$, of asteroids within a strip $(C, C + \Delta C)$ for $\Delta C = 4 \times 10^{-6}$ AU used in the target function $\Psi_{\Delta C}$ in Eq. (11). Symbols are the observed bodies $N_{obs}(C)$ with the assigned formal uncertainty $\sqrt{N_{obs}(C)}$; only the left branch of the family with asteroids having $a \leqslant a_c$ is used here. This is an averaged result where a_c is assumed to be uniformly distributed in the range (3.015, 3.025) AU. Broken solid line is our modeled family that minimizes the target function $\Psi_{\Delta C}$.

3.2.2. Yarkovsky/YORP family evolution model

Fig. 12 shows $\mathcal{D}(C)$ for the Eos family identified using the $V_c = 55$ m/s with $a \leqslant a_c$ (to avoid problems with the J9/4 MMR). The ordinate is the number $N_{obs}(C)$ of Eos members in the interval $(C, C + \Delta C)$, with $\Delta C = 4 \times 10^{-6}$ AU (there are 41 contributing bins/data points in this distribution). To match up the features in the plot as best as possible, we assumed a_c was uniformly distributed between 3.015 and 3.025 AU. These values are close to (221) Eos.

We find that $\mathcal{D}(C)$ has a maximum at $C \simeq -7.5 \times 10^{-5}$ AU. The value $\mathcal{D}(0)$ is roughly half of the maximum value. The error bars defined using $\sqrt{N_{obs}(C)}$ in each C bin. We discarded 3 objects, (1845) Helewalda, (8340) Mumma, (9711) Zeletava, from our analysis that had their $|C|$ value larger than 1.6×10^{-4} AU. In Fig. 3, they form a "triangle" of bodies with $a \leqslant 2.98$ AU and $H \leqslant 12$ that are separated from the bulk of the family. We suspect these objects are objects interlopers in the family. Indeed, in Section 4 we show that the first 2 are spectrally alien to the KTD-types common among Eos family members.

The $\mathcal{D}(C)$ maximum in Fig. 12 is produced by the unusual (a, H) distribution of the Eos family (Fig. 3), where small asteroids populate regions near the outskirts of the family and leave the center underpopulated. This distribution is unlikely to have been created by any reasonable ejection velocity field. Instead, we believe this artifact was produced by Yarkovsky/YORP evolution. Recall that the Yarkovsky–O'Keefe–Radzievskii–Paddack (YORP) effect (e.g., Rubincam, 2000; Vokrouhlický and Čapek, 2002; Bottke et al., 2002) is a variant of the Yarkovsky effect that can modify the rotation rates and obliquities of irregularly shaped bodies. In the Eos family, YORP preferentially tilts the obliquities of family members toward extreme values (Čapek and Vokrouhlický, 2004) that, in turn, help increase Yarkovsky da/dt rates. Hence, Yarkovsky/YORP should move small asteroids from the center of the family to more distant a values.

To test this hypothesis, we constructed a simple numerical model that tracked the evolution of test Eos family asteroids. Our goal was to quantitatively match the observed distribution $\mathcal{D}(C)$. Its main features and parameters are as follows:

- The initial orbits for our Eos family members were based on a test velocity distribution. The velocity components V_R, V_T, and V_N along the radial, transverse, and normal directions with respect to the parent body's orbit were given the same Gaussian distribution with standard deviation V_{SD}. We consider two models for V_{SD}: (i) it is a size-independent free parameter with values of the order $\simeq$0–100 m/s, or (ii) $V_{SD} = V$ (5 km/D), where V is a free parameter of the model. The number of fragments used in our simulations is the same as number of observed asteroids in the family. They were assigned the same H as the observed objects, with H converted to D using two methods (Tedesco et al., 2002): (i) all asteroids were given albedo $p_V = 0.13$ corresponding to the mean value of the Tedesco et al. Eos sample, and (ii) we assign random p_V to individual asteroids that follow the observed distribution of p_V (Fig. 16). In the latter case, we ran several simulations because the size of each asteroid is a statistical quantity. The results were then averaged over several simulations.
- The test asteroids are assigned initial diameters, orbital elements, obliquity (ϵ), and angular velocity of rotation (ω). The initial orientation of the spin axes is random in space. We assume ω follows a Gaussian distribution peaked at period $P = 8$ h (e.g., Binzel, 1988).
- The orbital evolution of each of the fragments is tracked individually, with Yarkovsky drift rates (e.g., Vokrouhlický, 1998, 1999):

$$\frac{da}{dt} = \kappa_1 \cos\epsilon + \kappa_2 \sin^2\epsilon. \tag{7}$$

  Here κ_1 and κ_2 are functions depending on surface thermal parameters and asteroid size. In accord with the numerical simulation above, we used the following set of thermal constants: thermal conductivity $K = 0.005$ W/m/K, specific heat capacity $C_p = 680$ J/kg/K, and surface/bulk densities of 1.5 and 2.5 g/cm^3, respectively. Equation (7) assumes (i) our model asteroids reside on a circular orbit and (ii) that we can use a restricted, linearized analysis to describe heat diffusion in the asteroid's surface layers. Our tests indicates that Eq. (7) is within a 2 of more sophisticated treatments of Yarkovsky/YORP.
- The two rotation state parameters, ϵ and ω, undergo YORP evolution according to

$$\frac{d\omega}{dt} = c_{YORP} f(\epsilon), \tag{8}$$

$$\frac{d\epsilon}{dt} = c_{YORP} \frac{g(\epsilon)}{\omega} \tag{9}$$

  (e.g., Vokrouhlický and Čapek, 2002; Čapek and Vokrouhlický, 2004). The f- and g-functions here are the median strength of the YORP torques derived by Čapek and Vokrouhlický (2004) for asteroids with the surface thermal conductivities described above. We also introduce a free parameter c_{YORP} by which we can multiply the f- and g-functions in Eqs. (8) and (9); this "fudge" factor helps account for the uncertainties in modeling the YORP effect.
- We assume that non-catastrophic collisions can reorient the spin vectors of the test asteroids with a timescale:

$$\tau_{reor} = B(\omega/\omega_0)^{\beta_1}(D/D_0)^{\beta_2}. \tag{10}$$

  Here $B = 84.5$ kyr, $\beta_1 = 5/6$, $\beta_2 = 4/3$, the reference size $D_0 = 2$ m, and the rotation frequency ω_0 corresponding to a rotation period of 5 h. This basic approach was pioneered by Farinella et al. (1998). We ignore for now the effects of disruptive collisions.

With a given initial configuration of the family, we run our code for a time T, ranging from 0.5 to 2 Gyr, and we let the family evolve by the Yarkovsky/YORP effects. Our solutions are a function of three parameters: T, V, and c_{YORP}. To determine the quality of the fit between the simulation and the observed Eos family, we define a pseudo-χ^2 target function

$$\Psi_{\Delta C} = \sum_{\Delta C} \frac{(N(C) - N_{obs}(C))^2}{N_{obs}(C)}. \tag{11}$$

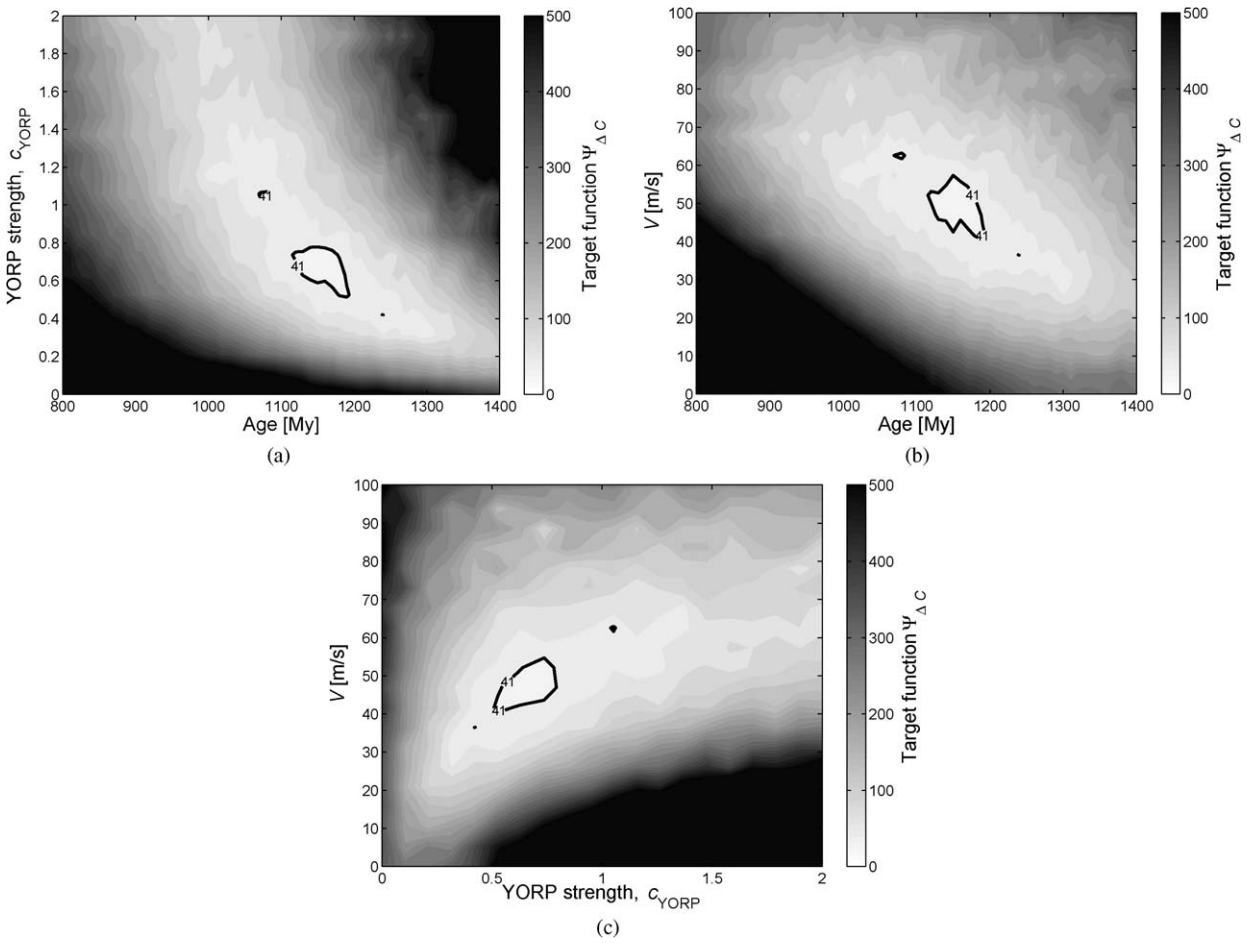

Fig. 13. Projection of the target function $\Psi_{\Delta C}$ onto planes defined by the model parameters: (a) T vs $c_{\rm YORP}$, (b) T vs V, and (c) $c_{\rm YORP}$ vs V (as in the previous figure $V_{\rm SD} = V$ is size-independent). Each time we plot the smallest $\Psi_{\Delta C}$ value along the ray of the third parameter (i.e., in the first case we fix T and $c_{\rm YORP}$ values of seek the minimum value for all tested values of V). We show shaded contours of $\Psi_{\Delta C}$ with the value indicated by a bar on the right; the best-fit value is $\Psi_{\Delta C} = 27.8$. This compares to 41 bins in ΔC, which set the formal 1σ uncertainty level (shown in bold curve).

The errors assigned to the number $N_{\rm obs}(C)$ in a given bin $(C, C + \Delta C)$ is $\sqrt{N_{\rm obs}(C)}$. $N(C)$ is the simulated number of asteroids in the appropriate C-bin. Our procedure seeks to minimize $\Psi_{\Delta C}(T, V, c_{\rm YORP})$ by varying the 3 parameters over a large range of values. Admissible solutions are characterized by $\Psi_{\Delta C}$ values of the order equal to the number of bins in C (41 in our case), while solutions giving much larger $\Psi_{\Delta C}$ are incompatible with the observed family.

3.2.3. Results

For simplicity, our first simulations assumed the test asteroids had a single albedo value $p_V = 0.13$ and that $V_{\rm SD} = V$ is size-independent. Fig. 13 shows contour plots of $\Psi_{\Delta C}$ projected onto several 2-D parameter planes: T vs $c_{\rm YORP}$, T vs V, and $c_{\rm YORP}$ vs V. The best-fit solution for $N(C)$, together with the observed data $N_{\rm obs}(C)$ and their formal error-bars, is shown in Fig. 12. Each time we picked the best $\Psi_{\Delta C}$-value along the suppressed dimension. The "critical" isoline value of 41 is plotted in bold; recall this value formally corresponds to solutions that barely match the observed family at the chosen 1σ-interval from all data points.

The best-fit solution is: $T = 1160^{+40}_{-100}$ Myr, $c_{\rm YORP} = 0.7^{+0.3}_{-0.2}$, and $V = 52^{+10}_{-14}$ m/s. Note that the 3 parameters are not uncorrelated in our solution, such that stronger YORP (i.e., larger $c_{\rm YORP}$) pushes the family age T to smaller values. The least correlated are $c_{\rm YORP}$ and V. The best-fit V is compatible with values expected from the hydrocode modeling. The initial family thus had about half of its current a spread.

The $c_{\rm YORP} \simeq 0$ value is strongly incompatible with observations; this means that YORP is needed to match observations. Its strength, however, is poorly constrained. The best-fit value of the target function (11) is $\Psi_{\Delta C} = 27.8$, smaller than 41 and statistically significant (assuming our approximations are reasonable; note the value of the standard goodness-of-fit parameter $Q = 0.89$ for our solution, see, e.g., Press et al., 1999).

Figs. 14 and 15 show the best-fit solution for $N(C)$ and 2-D contour plots of the target function $\Psi_{\Delta C}$ in case of our more refined model where $V_{\rm SD} = V$ (5 km/D). Now V is a solved-for parameter with the ejection velocity set for $D = 5$ km fragments. Our best-fit solution is: $T = 1150^{+150}_{-100}$ Myr, $c_{\rm YORP} = 1.1^{+0.9}_{-0.7}$, and $V = 93^{+25}_{-20}$ m/s. The uncertainty limits are derived from the $\Psi_{\Delta C} = 41$ contour plot. The minimum target function, $\Psi_{\Delta C} = 26.2$, is below the admissible limit of 41; hence

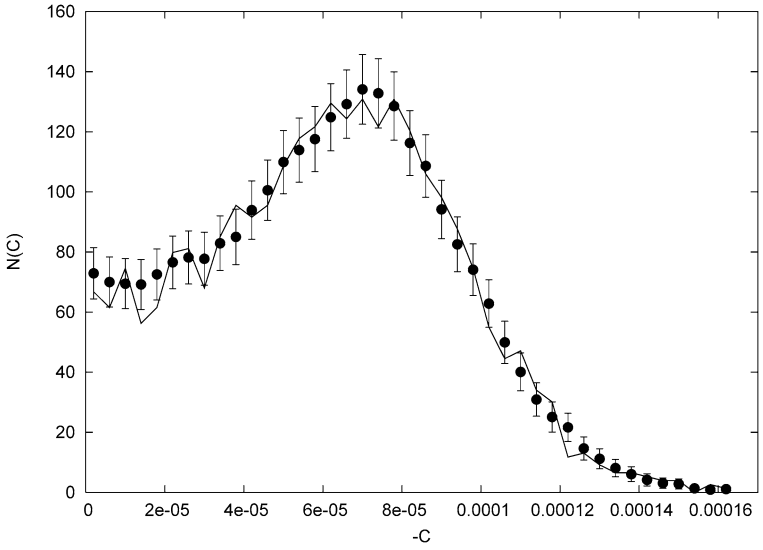

Fig. 14. The same as in Fig. 12 but here for the model where $V_{\rm SD} = V\ (5\ {\rm km}/D)$ is size-dependent.

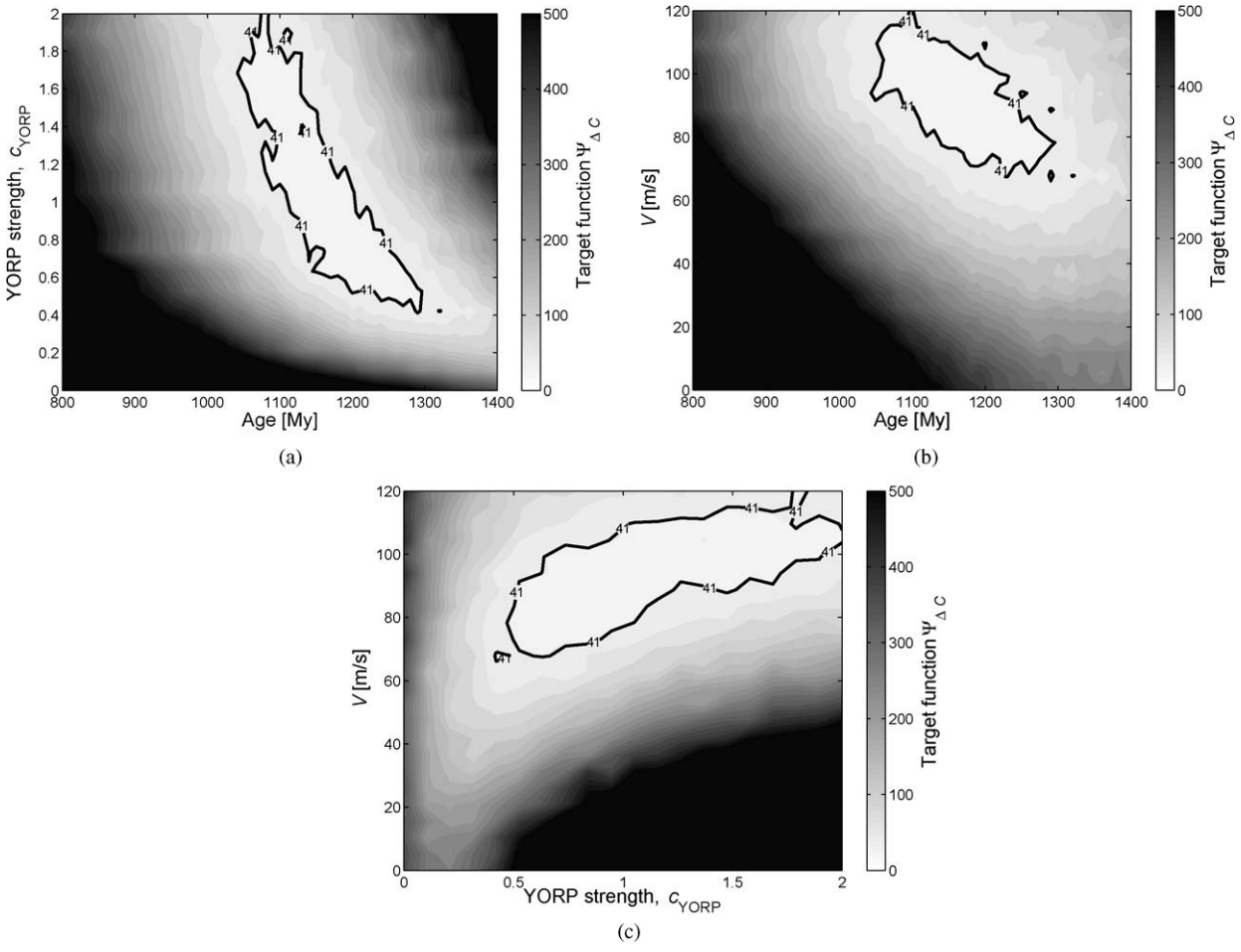

Fig. 15. The same as in Fig. 13 but here for the model where $V_{\rm SD} = V\ (5\ {\rm km}/D)$ is size-dependent. The best-fit value is $\Psi_{\Delta C} = 26.2$.

we consider it statistically significant and slightly better than the previous solution. The general features of the solution are similar to the previous one. In our opinion, two results are of particular interest: (i) the estimated age of the Eos family consistently spans the same interval of values, and (ii) the estimated YORP strength is within a factor 0.5–1 of the modeled value by Čapek and Vokrouhlický (2004).

In the previous tests we assumed the luminosity of the Sun was constant. Evolutionary models of the solar interior, however, suggest the Sun was ∼25% fainter some 4 Gyr ago (e.g.,

Bahcall et al., 2001, Table II). A smaller radiation flux in the past should produce weaker thermal Yarkovsky/YORP effects and thus may modify our conclusions. For that reason, we have rerun our previous simulations to account for a time-variable solar luminosity ($L(t)$):

$$L(t) \simeq L_0 \left[1 + 0.3 \left(1 - \frac{t}{t_0} \right) \right]^{-1}, \tag{12}$$

where L_0 is the current solar luminosity, $t_0 \simeq 4.57$ Gyr is the age of the Sun, and t is time (in Gyr) measured from the origin of the Solar System (e.g., Bertotti et al., 2003, Chap. 7). Our results indicate that while the best-fit values for $c_{\rm YORP}$ and V are comparable to our previous results, the estimated age T of the family is slightly increased: $T = 1200^{+120}_{-100}$ Myr. Note that according to Eq. (12), the mean solar luminosity over the past Gyr was about 4% lower than today, which corresponds to a $\simeq$4% increase in the Eos family's age. Thus, for a moderately young family like Eos, the effect of a fainter Sun in the past appears to be smaller than other model uncertainties.

Finally, we tested how our results change as a function of asteroid geometric albedo p_V. To do so, we used a p_V distribution determined for 98 Eos members (selected from our nominal family at HCM $V_{\rm cut} = 55$ m/s) by Tedesco et al. (2002), Fig. 16. Note that the data show a considerable spread about the mean value of $p_V = 0.13$, with some skew toward values that are smaller than the median value. We ran 10 simulations similar to those above using the mean ejection velocities of fragments inversely proportional to their D (our second model above). Our asteroid diameters were determined by randomly assigning p_V values.

We found that our best-fit values of $\Psi_{\Delta C}$ ranged from 17 to 26, which means our solutions were a reasonable fit with observations. Considering the mean value of the best-fit solution for each of the free parameters (weighted by the best-fit value of the target function), and an envelope of the $\Psi_{\Delta C} = 41$ region in the parametric space, we obtain $T = 1300^{+150}_{-200}$ Myr, $c_{\rm YORP} = 0.7^{+1}_{-0.5}$, and $V = 70^{+20}_{-20}$ m/s. In comparison with the fixed albedo $p_V = 0.13$ model, we find that our family's age T slightly increased. This is because lower albedo values imply larger asteroid sizes and thus slower Yarkovsky da/dt rates (and slower YORP torques).

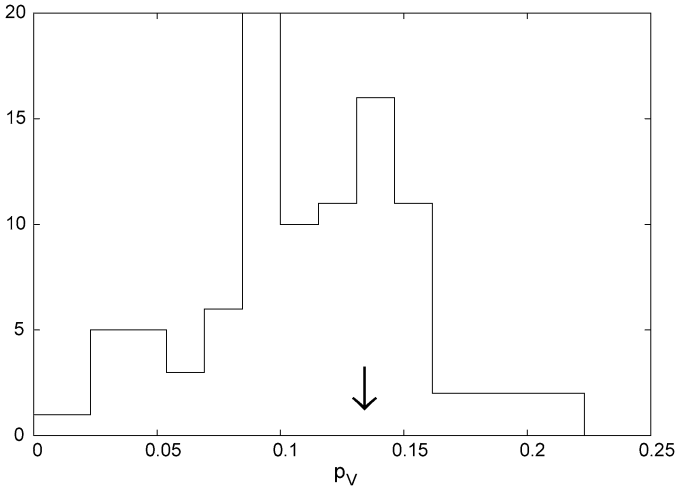

Fig. 16. Distribution of the geometric albedo values p_V for Eos members determined by Tedesco et al. (2002); abscissa is p_V, ordinate is number of asteroids with p_V in a given bin. The arrow indicates the mean value.

3.3. Asteroids in the z_1 secular resonance

So far, there has been little work on how high-order secular resonances affect the long-term fast of asteroid families. In part, this is because the topic is analytically and numerical challenging from the orbital dynamics point of view. Milani and Knežević (1990, 1992, 1994) and Knežević and Milani (2003) have been pioneers in the investigation of high-order secular resonances. They found that the Eos family is intercepted by the $z_1 = g + s - g_6 - s_6$ resonance.[5] While no significant effects on family evolution are expected on Myr timescales, Milani and Knežević (1990, 1992) speculated that they might affect the structure of the Eos family over longer timescales. Note that this hypothesis has been cited several times over the last 15 years (e.g., Zappalà et al., 1990; Marzari et al., 1995) but no one has yet tested it.

The second reason why the high-order secular resonances received a little attention so far is that the asteroid families were assumed by many to deviate from simple models for other, more obvious reasons such as uncertain geometry of the initial velocity field. These were expected to mask any noticeable trace of the dynamics in weak secular resonances. New results, however, suggest the asteroids drifting by Yarkovsky effect into these resonances can follow unusual orbital paths. For example, Bottke et al. (2001) showed that Koronis family asteroids experience a significant jump in proper eccentricity ($\simeq$0.025) when they drift into (and interact with) the $g + 2g_5 - 3g_6$ secular resonance.

Below we will show that the shape of the Eos family has also been affected by secular resonances. As asteroids migrate in the proper element space by the Yarkovsky effect, they become captured by the z_1 secular resonance and are driven to a specific region at the outskirts of the family (Fig. 4).

3.3.1. Theoretical basis

A fundamental model used to track a perturbed asteroid's motion is the restricted three-body problem of Sun–Jupiter–asteroid (e.g., Morbidelli, 2002). Many aspects of asteroid motion, including fine perturbations, can be studied within this framework. Each of the various problems, such as motion in/

[5] This resonance causes the secular angle $\varpi + \Omega - \varpi_6 - \Omega_6$ to librate rather than circulate on a typical timescale of 3–5 Myr; here ϖ is longitude of pericenter and Ω is longitude of node of the asteroid, while ϖ_6 and Ω_6 are the same parameters for Jupiter. In an analytical theory, such as Milani and Knežević (1990, 1992), the $g+s-g_6-s_6$ frequency appears as a small divisor associated with this resonance. More in general, a z_k resonance corresponds to a divisor $k(g - g_6) + s - s_6$ with an integer k. All z_k resonances are secondary modes of the $g - g_6$ secular resonance and thus have larger width than other nonlinear secular resonances of the same order (e.g., Milani and Knežević, 1994; Carruba et al., 2005).

near mean motion or secular resonances, is best understood if properly chosen variables are used. We thus start with a brief review of the variables tailored to understand the z_1 resonance.

The restricted three-body problem is a 4-degree of freedom autonomous system with the first 3-degrees describing 3-D motion of the test body (asteroid) and the last degree being Jupiter's orbital longitude (removing time-dependence due to Jupiter's motion). In a Hamiltonian approach, the asteroid-related degrees of freedom can be described using Delaunay variables $(L, G, H; l, g, h)$ or variables derived from them by canonical transformations (e.g., Morbidelli, 2002). For instance, we can choose

$$\begin{pmatrix} L & l \\ G & g \\ H & h \end{pmatrix} \rightarrow \begin{pmatrix} \Lambda = L & \lambda = l + g + h \\ \Sigma = L - G & \sigma = -g - 2h \\ \Theta = 2G - H - L & \theta = -h \end{pmatrix}, \qquad (13)$$

where the new canonical variables $(\Lambda, \Sigma, \Theta; \lambda, \sigma, \theta)$ replace the original Delaunay set.

Representations of Jupiter's motion become more involved when we include perturbations with Saturn; these produce secular variations of its orbital elements. This extends the problem by at least 3 degrees of freedom (e.g., Moons et al., 1998; Morbidelli, 2002); notably nonsingular elements $(e' \cos \varpi', e' \sin \varpi'; \sin(I'/2) \cos \Omega', \sin(I'/2) \sin \Omega')$ of Jupiter are going to be expressed as harmonic functions of the secular angles $\lambda_5 = g_5 t$, $\lambda_6 = g_6 t$, and $\lambda_{16} = s_6 t$ (here g_5, g_6, and g_{16} are the corresponding fundamental frequencies of the planetary system; e.g., Morbidelli, 2002). The conjugated momenta to these angular variables are Λ_5, Λ_6, and Λ_{16}. Using another canonical transformation

$$\begin{pmatrix} \Sigma & \sigma \\ \Lambda_6 & \lambda_6 \\ \Lambda_{16} & \lambda_{16} \\ \dots & \dots \end{pmatrix} \rightarrow \begin{pmatrix} -\Sigma & -\sigma - \lambda_6 - \lambda_{16} \\ \Sigma - \Lambda_6 & -\lambda_6 - \lambda_{16} \\ \Lambda_6 - \Lambda_{16} & -\lambda_{16} \\ \dots & \dots \end{pmatrix}, \qquad (14)$$

we obtain variables suitable to analyze orbital motions in the z_1 resonance because $\Sigma' = -\Sigma$ and $\sigma' = -\sigma - \lambda_6 - \lambda_{16}$ appear to be resonant momentum and critical argument of this secular resonance.

In a simplified model where all other degrees of freedom are eliminated by averaging, the resonance becomes represented by a 1-D model in resonant variables (Σ', σ'). In particular, σ' circulates outside the resonance with secular frequency $-\dot{\sigma} - g_6 - s_6$ (overdot is a time derivative), while σ' librates inside the resonance, i.e., near the hypersurface $\mathcal{Z}_1$: $-\dot{\sigma} - g_6 - s_6 \simeq 0$. Because $\Sigma' = \sqrt{a}(1 - \sqrt{1 - e^2})$, and a is constant due to the eliminated variable λ, the resonance produces long-term variations in eccentricity e. Moreover, because Θ is also constant, due to the elimination of θ, we have a quasi-integral $\sqrt{a(1 - e^2)}(2 - \cos I)$. Thus the long-term variations of orbital eccentricity e and inclination I are resonantly coupled and the inclination is given long-term variations.

Difficulties arise when non-gravitational forces like the Yarkovsky effect are included in the model. In the simplest representation, we can only retain the major secular effect, namely a steady a change. Because the characteristic timescale for this perturbation is long, even when compared to secular dynamics timescales in the weak z_1 resonance, one must still assume a is constant during one resonant cycle of σ' and investigate the evolution of the system under slowly (adiabatically) changing parameter a. This approach could, in principle, yield capture probabilities in the z_1 resonance for bodies with different $\mathrm{d}a/\mathrm{d}t$ rates. Once in the resonance, however, the asteroids show coupled oscillations in e and I superposed over a slow migration along the $\mathcal{Z}_1$ hypersurface. This takes place until the asteroid reaches conditions that allow it to jump out of the resonance.

3.3.2. z_1 resonance in the Eos family

To examine evolution inside the z_1 resonance, we first need to identify those Eos family asteroids currently inside the resonance. This was accomplished by taking our nominal family with 4394 members and numerically integrating their orbits for 10 Myr. Our goal was to compute the behavior of the critical angle σ'. To do this accurately, we excluded Yarkovsky forces from our integrations. We output the mean orbital elements of the asteroids every 1.5 kyr using Fourier filtering of high-frequencies taken from the osculating orbital elements. The mean orbital elements were then processed to identify asteroids residing in the z_1 resonance. In particular, we used a running window filter that was 750 kyr wide and had steps of 100 kyr.

In each interval, we Fourier-analyzed the time series of the non-singular orbital elements and determined the frequency and phase of the proper and forced terms. Among the forced terms, we were principally interested in isolating the g_6 and s_6 frequencies and their associated phases. The phases were used to construct the critical angle σ' of the resonance, where ϖ and Ω are substituted by the phases of the corresponding proper terms in non-singular orbital elements, and ϖ_6 and Ω_6 are the phases of the corresponding forced terms. We replaced the momentum Σ' with the frequency combination $g + s - g_6 - s_6$ and plotted asteroid tracks in the configuration space of these two variables.

Fig. 17 shows several examples including Asteroid (221) Eos that is currently trapped in the z_1 resonance (e.g., Milani and Knežević, 1990, 1992). We show the motion of asteroids whose (i) σ' librates at small amplitudes, which allows them to residing near the center of the resonance, (ii) σ' alternates between libration and circulation, which allows them to reside near the separatrix of the resonance, and (iii) σ' circulates. Typical libration periods of σ' inside the resonance are 3–5 Myr, with the resonance width $\sim$0.8 arcsec/yr.

Fig. 4 helps to translate this information into a portion of the proper element space affected by the z_1 resonance. Interestingly, we find that it stretches over a non-negligible fraction of the Eos family. We find that 13% (575 out of 4394) of all Eos family members are captured inside this resonance. (As an aside, we also found that $\simeq$1.5% of Eos family members both reside and librate in the $g + s - g_5 - s_7$ secular resonance. This is because this resonance is much weaker than the z_1; Milani and Knežević, 1990, 1992.) Fig. 18 shows the distribution of the critical angle σ' of all 4394 asteroids associated with the family. Unlike previous studies, we show the distribution of σ' separately for Eos members residing inside (top) and outside

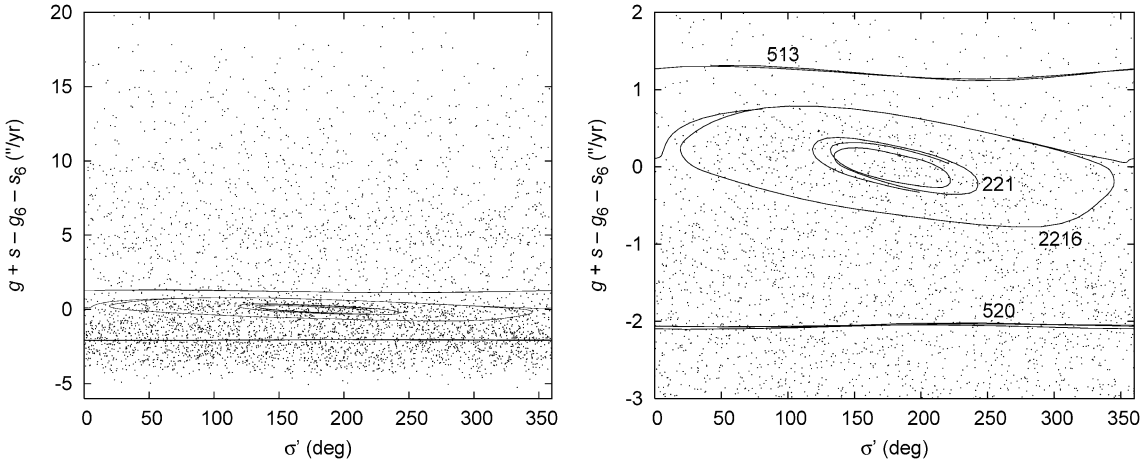

Fig. 17. Configuration space of the z_1 secular resonance: critical angle σ' at the abscissa and secular frequency $g + s - g_6 - s_6$ on the ordinate. Left: all family asteroids included; right: zoom of the previous figure near z_1 resonance zone. Solid curves show evolution tracks of several Eos-family asteroids during our 10 Myr orbital integration (high-frequencies have been eliminated). The innermost librating orbit is (221) Eos itself, while other asteroids show and example of transitions between libration and circulation—(2216) Kerch—and circulations—(513) Centesima and (520) Franziska. Dots are current position of Eos asteroids (HCM family with $V_c = 55$ m/s). The negative value of $g + s - g_6 - s_6$ frequency occurs when orbital semimajor axis is smaller than the z_1 libration center for given value of the eccentricity and inclination; thus the bulk of the family (adhering eventually to the J7/3 MMR; see Fig. 4) projects to this part of our plot.

(bottom) the z_1 resonance. The first is non-uniform because σ' values are naturally confined near the stable resonant point at 180°. However, when non-resonant Eos members are considered, we find that σ' distribution is uniform up to random fluctuations.

For sake of completeness, we also show a σ' histogram for the 58 Eos family asteroids known to Brouwer (1951): dashed histogram in both panels of Fig. 18. Like Brouwer, we also find they show some degree of non-uniformity. The reason is that large asteroids near (221) Eos are preferentially located inside the z_1 resonance (the same applies, to a lesser degree, to data reported by Milani and Knežević, 1992). Hence the previously reported non-uniform distribution of σ' is a selection effect unrelated to the age of the family.

We found that the z_1 produced no significant instability among Eos family members over our 10-Myr integration. Nevertheless, as shown in Fig. 19, it produces a non-negligible spread of the family in eccentricity and inclination, likely contributing to solve the old problem of the Eos family (see Section 1). This is partly surprising given the weakness of the resonance: for a near-separatrix case, such as (2216) Kerch, the synthetic proper eccentricity, determined from an integration spanning $\simeq$1 Myr, may oscillate in time by nearly 0.02, about a half of the total eccentricity extension of the family. The same applies to the inclination.

The role of the z_1 resonance changes and strengthens, however, when Yarkovsky forces are taken into account. As demonstrated by our numerical integration above (see also Vokrouhlický and Brož, 2002), migrating asteroids encountering the z_1 resonance can become captured for several tens to hundreds of Myr. During this time, its orbital parameters slide along the z_1 resonance while its semimajor axis changes. Hence, Eos family members moving toward the Sun experience a decrease in their mean a, e, I values. This populates the anomalous tail of the Eos family (Section 2). Investigating Eos family members whose proper elements satisfy $a \leqslant 3.01$ AU, $e \leqslant 0.065$, and $\sin i \leqslant 0.17$, we found that 67% (246 out of 366) reside in the z_1 resonance. This high fraction, when compared to the rest of the Eos family, suggests they reached their current orbits via an interaction between the resonance and Yarkovsky-induced drift.

4. Additional data and observations

In order to check our results, we conducted spectroscopic observations of about a dozen asteroids in the Eos zone. Our objective was to determine whether particular asteroids were related to the KTD-types seen among the majority of Eos family members or whether they were more likely to be interlopers in the family. In one case, we investigated asteroids located inside the z_1 secular resonance with anomalously small values of proper e, i as compared to the other Eos family members (Section 3.3). In a second case, we examined suspected interlopers in the Eos family that were far from the family members plotted in Fig. 3. We start by describing our own observations in Section 4.1. We then add to this database using an updated SDSS color information in Section 4.2.

4.1. Spectroscopy

4.1.1. Asteroids inside the z_1 resonance

Table 3 summarizes our target asteroids and the observational circumstances. The asteroids inside the z_1 stream are generally small, so their spectroscopy is challenging even with moderately large instruments. Our sample of the observed asteroids is random, mainly derived from observational possibilities from available instruments and times. The Kitt Peak National Observatory (KPNO) and Palomar observations reported here were acquired both through a dedicated program for this work and also as targets of opportunity during the ongoing Small Main-Belt Asteroid Spectroscopic Survey (SMASS). The KPNO observations used the RCSP spectrometer on the

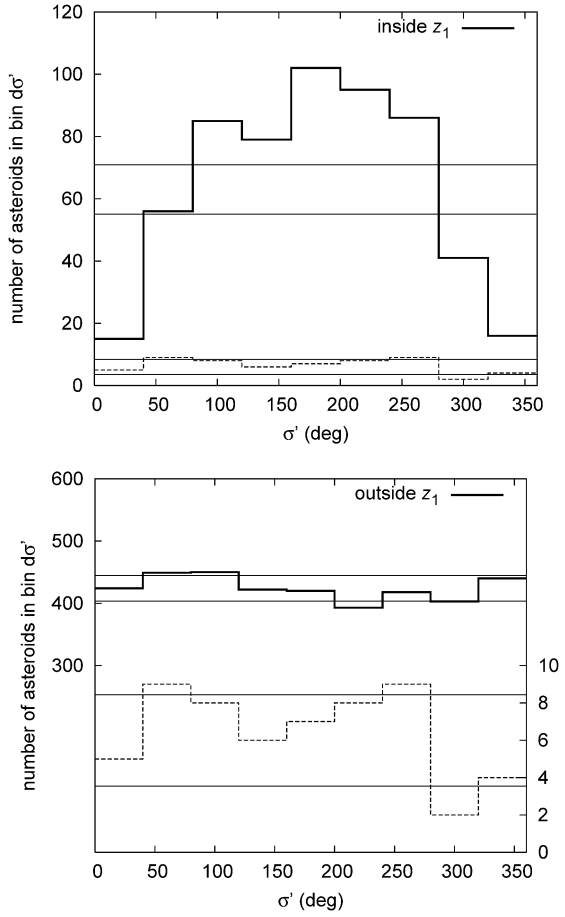

Fig. 18. Distribution of the critical angle σ' values determined for members of our nominal Eos family (solid line and left ordinate). Previous analyses, e.g., Brouwer (1951) or Milani and Knežević (1992), found it non-uniform and suspected a young age of the family; the dashed curve (and right ordinate in the bottom panel) in both figures reconstructs the similar quantity for the 58 Eos members known to Brouwer (1951). Here, we show that (i) with modern data, many more asteroids added in the family, the distribution is fairly uniform, and (ii) the anomaly reported by the previous studies is due to selecting asteroids preferentially inside the z_1 resonance, for which σ' is limited to their libration interval (and the σ' values are preferentially found near extremes of the libration cycle). This is proved by showing the σ' distribution separately for asteroids which were found to librate in the z_1 resonance (top), and for those which are outside the resonance (bottom). In each case the horizontal lines show the $\sqrt{N_m}$-uncertainty strip about the mean value N_m of the uniform distribution. In the bottom panel, where asteroids residing in the z_1 were eliminated, the fluctuations of N_m fall in this uncertainty strip.

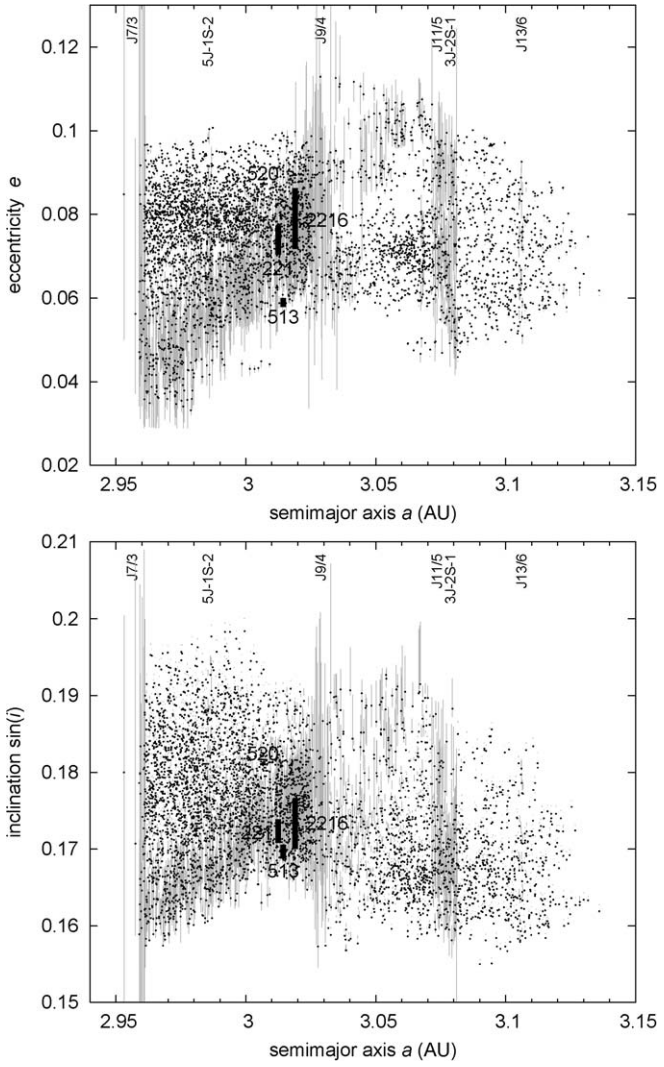

Fig. 19. Stability of the proper elements for the nominal Eos family. In black dots we show the nominal family from proper elements of the AstDyS catalogue, used also in previous parts of this paper. In gray lines we show variation of the synthetic proper elements determined from our 10-Myr integration for all 4394 members. In particular, the gray intervals delimit minimum and maximum values of the proper elements (eccentricity e and inclination $\sin i$) determined by Fourier filtering on a running 700-kyr wide window in our integration. The principal diagonal gray strip in both plots is the effect of the z_1 secular resonance. In this case, the period of e and $\sin i$ oscillation is several Myr (e.g., Fig. 17). Note the amplitude of the z_1 driven variation of the proper orbital elements is surprisingly large (as opposed to the resonance weakness) and it amounts to a fair fraction of the whole dispersion of the family in the appropriate elements. The thick bars are the four asteroids from Fig. 17; obviously, the largest amplitude of the oscillation occurs for (2216) Kerch, which resides near separatrix of the z_1 resonance. We also indicate effects of several MMRs, whose nomenclature is indicated at top. The most significant are effects of J7/3 and J9/4, but we can notice also J11/5 and the three-body resonance 3J–2S–1.

Mayall 4-m telescope, generally covering the spectral range 500–920 nm, and the Palomar observations used the Double Spectrograph on the Hale 5-m telescope and generally covered the spectral range 320–950 nm. Details of the observations and reductions can be found in Binzel et al. (2004), which used the same telescopes and instruments and had identical data reduction and analysis techniques. To summarize, well-known solar-type stars were observed frequently during the night interspersed with target objects in order to account for the influence of the solar spectrum and the terrestrial atmosphere on the target asteroids. Commonly used IRAF routines and packages[6] were used to extract the spectra of the asteroids and stars, and a set of mean extinction coefficients appropriate for each observing site was used for additional corrections. The resulting asteroid/star ratios were then tied into the spectral taxonomy of Bus and Binzel (2002a, 2002b).

Fig. 20 shows the collected reflectance spectra for our 4 objects, indicating three are T-class and one—(62948) 2000

[6] See Tody (1986) and http://iraf.noao.edu/iraf-homepage.html for details.

Table 3
Observations of the asteroids in the z_1 resonance zone (Fig. 20)

Asteroid	a (AU)	H	V_c (m/s)	ST	Date	Site
(20845) 2000 UY102	2.979	12.3	48	T	20-Jan-02	KPNO
(21211) 1994 PP36	2.976	13.41	48	T	20-Jan-02	KPNO
(33780) 1999 RU171	2.973	13.05	48	T	06-Mar-02	KPNO
(62948) 2000 VE32	2.960	13.73	58	X	22-May-03	KPNO

Notes. 1. Orbital data and family association (2nd through 4th columns): a is the proper semimajor axis, H absolute magnitude (AstOrb source), V_c is the critical HCM velocity cut-off at which the asteroid associates with the family. 2. ST stands for the inferred spectral type from our observation (5th column). 3. Observational circumstances (6th through 7th columns): UT date, observatory (KPNO stands for the 4-m Kitt Peak National Observatory telescope).

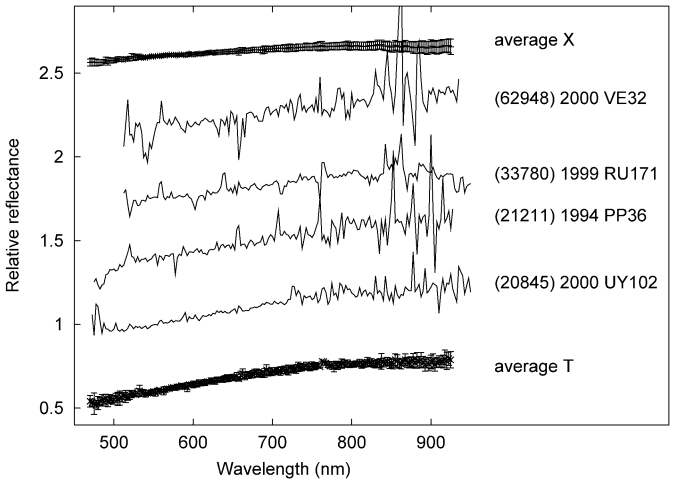

Fig. 20. Relative reflectance spectra, normalized to unity at 550 nm, of asteroids in Table 3. For (20845) UY102 the ordinate is in order, while for the other objects we arbitrarily shifted the data each time by 0.4 for visibility. For sake of comparison, we also show average reflectance spectra of T- and X-type asteroids from the SMASS dataset (Bus and Binzel, 2002a, 2002b, and http://smass.mit.edu).

VE32—is an X-type. As discussed in Section 2.2, the T types are compatible with the bulk Eos family and thus we interpret these 3 objects as potential Eos members that were pushed to their present orbits by Yarkovsky forces. The X-type asteroid in the same zone appears to be an interloper object caught in the z_1 resonance. The ∼25% fraction of alien asteroids in our observing sample, though not statistically significant, may correspond to the overall ∼25–30% interloper fraction inside the Eos family inferred from spectroscopic observation of large members (see Section 2.2). In fact, we might even expect higher interloper fraction among small Eos members because of shallower exponent of the families' size distribution as compared to the background population (Morbidelli et al., 2003).

4.1.2. Suspected interlopers

Next we comment on observations of suspected interlopers in the Eos family (Table 4). In this case we used three sites and instruments to collect the data: (i) the 1.52-m European Southern Observatory (ESO) telescope at La Silla, (ii) 4-m telescope at KPNO, and (iii) 5-m telescope at Palomar.

Table 4
Observations of the suspected interlopers in the Eos family (Fig. 21); data as in Table 3

Asteroid	a (AU)	H	V_c (m/s)	ST	Date	Site
(251) Sophia	3.095	9.84	55	L	22-May-03	KPNO
(1755) Lorbach	3.092	10.74	58	T	21-Jan-02	KPNO
(2193) Jackson	3.108	10.31	60	X	23-Mar-02	La Silla
(3937) Bretagnon	3.066	11.45	55	X	22-Mar-02	La Silla
(4431) Holeungholee	3.060	11.4	65	X	20,21-Mar-02	La Silla
(8340) Mumma[a]	2.970	11.9	48	D	23-Nov-01	Palomar
(11993) 1999 XX	3.086	12.86	49	Xk	22-May-03	KPNO
(27789) 1993 BB7	3.072	12.18	45	K	08,11-Nov-02	La Silla
(36151) 1999 RG193	3.087	12.45	52	Xk	22-May-03	KPNO

Note. Additional sites: Palomar (60-inch Palomar telescope), La Silla (1.52-m ESO telescope located at La Silla, Chile, operated under the agreement with the CNPq/Observatório Nacional, Rio de Janeiro).

[a] (8340) Mumma is also the largest asteroid in the z_1 stream from the Eos family.

The observations carried out at La Silla were an extension of the S^{3}OS^2 survey (Lazzaro et al., 2004) during two observational runs in March and November 2002. The ESO 1.52-m telescope was equipped with a Boller and Chivens spectrograph and a 2048 × 2048 pixels CCD detector with a readout noise of 7[e^- rms] and square pixels of 15 μm. A grating of 225 g/mm with a dispersion of 33 nm/mm in the first order was used. This configuration resulted in an useful spectral range of 490–920 nm with a FWHM of 1 nm. The spectra were taken through a 5-arcsec slit oriented in the East–West direction. The spectral data reduction was performed using the IRAF package and the classical procedure with averaged bias and dome flat-fields. Wavelength calibration was performed using a He–Ar lamp, which spectrum was obtained several times during each night. The spectra were corrected for airmass by using the mean extinction curve of La Silla (Tüg, 1977). Different solar analogs (Hardorp, 1978) were observed in each observational run in order to compute reflectivities. Tests made using different solar analogs produced differences in the reflectance spectra smaller than 1%/100 nm. The solar analogs HD44594 and HD20630 were used in the March and November run, respectively. The obtained asteroid spectra have been normalized around 550 nm by convention.

Fig. 21 folds all acquired spectra into a common frame with a necessary shift in the reflectance scale for visibility. The lowest shown are three X-type objects, certainly spectrally alien to the Eos family. The same holds for (251) Sophia, a large target seemingly offset in semimajor axis from the family members of comparable sizes (Fig. 22). Our data make us classify this target as L-type, dissimilar to the main KTD sequence in the family. All these four objects are our searched, high-C interlopers. Further objects require closer discussion.

Asteroid (8340) Mumma is the only object we observed with semimajor axis smaller than $a_c = 3.02$ AU and a high value of the C parameter (see Fig. 22 where we summarize positions of our observed targets in the (a, H) projection; an X-type Asteroid (1845) Helewalda was added here for sake of interest, Mothé-Diniz et al., 2005). We note that this is the largest ob-

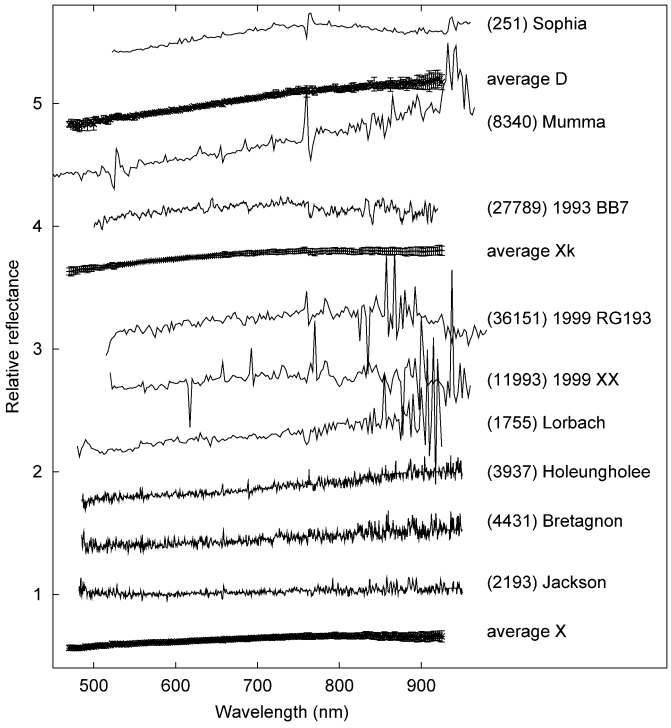

Fig. 21. Relative reflectance spectra, normalized to unity at 550 nm, of asteroids in Table 4. For (2193) Jackson the ordinate in order, while for the other objects we arbitrarily shifted the data each time by 0.4 for visibility. Noisier data for some objects reflect their relative faintness. For sake of comparison, we also show average reflectance spectra of X-, Xk-, and D-type asteroids from the SMASS dataset (Bus and Binzel, 2002a, 2002b, and http://smass.mit.edu).

ject located inside the z_1 secular resonance. With $a = 2.97$ AU, it is largely offset from the family center, so that the Yarkovsky forces could not have transported it to its location from the family center in $\simeq$1 Gyr. For these reasons, we believe it is an interloper. We find (8340) Mumma a possibly D-type object, though its spectral steepness sets it apart from other D-type asteroids embedded inside the Eos family. In the next section, we use SDSS data to show that (8340) Mumma is likely to be an interloper.

Asteroid (27789) 1993 BB7 has a spectrum resembling that of the K-type asteroids, suggesting that it is an Eos family member even though it has a large value of $C = 1.77 \times 10^{-4}$ AU. Fig. 22 suggests this object is at the furthest extreme of the family. We speculate that its C value might have been enhanced by a favorable initial orbit and/or jumping through the J9/4 MMR on its way toward larger semimajor axis values. Indeed, the finite width of this resonance, 0.005–0.01 AU (Figs. 7 and 8), helps dispersing family members on far side of the J9/4 MMR.

Of the 2 Xk-type objects, (11993) 1999 XX and (36151) 1999 RG193, the first lies close to the periphery of the family. Its flat spectra, however, makes a match less likely. The most intriguing case is that of (1755) Lorbach, a T-type asteroid well beyond a reasonable association with the family (Fig. 22); note that this asteroid is associated with the Eos family at $V_c = 58$ m/s. T types are not exclusive members of the Eos family but rather are found throughout the main belt. This suggests that (1755) Lorbach could be an interloper.

Searching two different spectroscopic databases, SMASS and S^{3}OS^2, we found 49 T-type asteroids. Out of this sample, 5 are members of the Eos family. Note that an additional 22 T-type Eos members are known through dedicated observing programmes (Doressoundiram et al., 1998; Mothé-Diniz et al., 2005), but we restrict our sample to the general purpose databases described above. The zone surrounding the Eos family contains another 12 T-type asteroids.[7] This suggests the background zone near the Eos family contains a non-negligible number of T-type asteroids, of which (1755) Lorbach may be a member.

4.2. SDSS data

In addition to narrow-band spectroscopy, we also examined the SDSS database containing 5-color data in order to characterize smaller asteroids inside the Eos family. We use the same methodology and data analysis as in Nesvorný et al. (2005a), though here we take advantage of the third, updated release of the SDSS data. This source contains five color information about 43424 objects. We found 985 Eos members in this database, which were used to construct normalized reflectance spectra and compute their principal components PC_1 and PC_2 (see Eq. (1) in Nesvorný et al., 2005a). For the final analysis, we choose only 499 asteroids with formal PC_1 and PC_2 errors smaller than 0.1.

Fig. 23 shows our results. The left panel gives the mean 5-point spectrum (dashed line) together with a formal standard deviation strip (shaded zone). The overall shape is a good match to the T-type classification. This comparison, however, may be partially flawed because of the unique properties of the SDSS broad-band filters. Namely, the long-wavelength SDSS z filter spans a rather broad wavelength interval centered about 909.7 nm (e.g., Fukugita et al., 1996) and it smears the absorption feature near 0.9 μm that is crucial for the spectral taxonomy in optical bands.

For this reason, we projected the family into the principal component axes (Fig. 23, right panel). Though some scatter is noticeable here, the Eos members appear to constitute a distinct cluster in these variables. Assuming the Eos cluster represents a formal relation of the two principal component parameters PC_1 and PC_2, we may determine confidence levels corresponding to this relationship (e.g., Bertotti et al., 2003, Section 20.5). In Fig. 23 we show the ellipses of 90 and 99% Eos membership based of our analysis. Asteroids close to these limits, or beyond them, are weakly connected with the bulk of the family and likely represent outliers.

We searched for large objects close to or beyond the 90% confidence level which correspond to a large $|C|$ from Eq. (5), i.e., objects detached from the family in (a, H). We found 4 cases of interest (shown as crosses in Fig. 23). (4843) Megantic and (4431) Holeungholee, denoted 3 and 4, have both been classified X-types using narrow-band spectroscopy (Lazzaro et

[7] These are: (96) Aegle, (465) Alekto, (596) Scheila, (717) Wisibada, (979) Ilsewa, (986) Amelia, (987) Wallia, (1006) Lagrangea, (1209) Pumma, (1306) Scythia, (2813) Zappala, (2929) Harris.

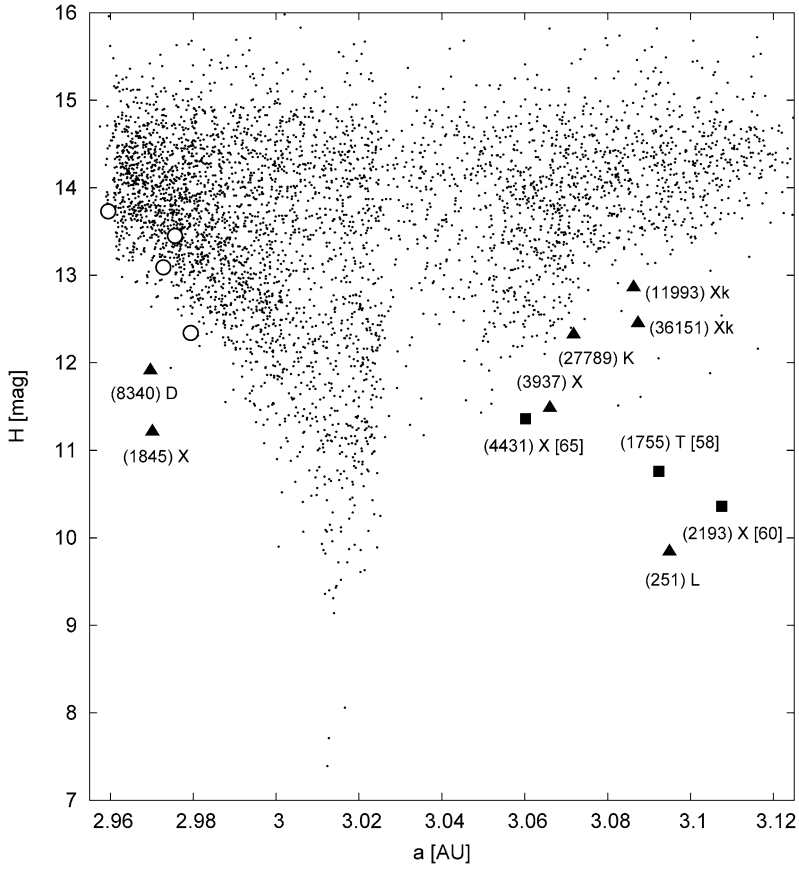

Fig. 22. The nominal Eos family, $V_c = 55$ m/s, projected onto the plane of proper semimajor axis a and absolute magnitude H—dots. Symbols indicate position of asteroids whose spectra are reported in the paper: (i) open circles are objects inside the z_1 secular resonance (Table 1 and Fig. 20), all T-types except for (62948) 2000 VE32 which is X-type and resides nearest to the J7/3 MMR; (ii) triangles are objects nominally associated with the family but which correspond to extremal values of C parameter from Eq. (5), such that $|C| \geqslant 1.6 \times 10^{-4}$ AU, which are suspected interlopers; (iii) squares are the same as blue in (ii) but for asteroids associated with the Eos family at HCM cut-off velocity larger than 55 m/s. In the latter two classes we show the asteroid designation, spectral type and, in the (iii) case, the HCM cut-off velocity at which the body associates with the family (the number in squared brackets in meters per second).

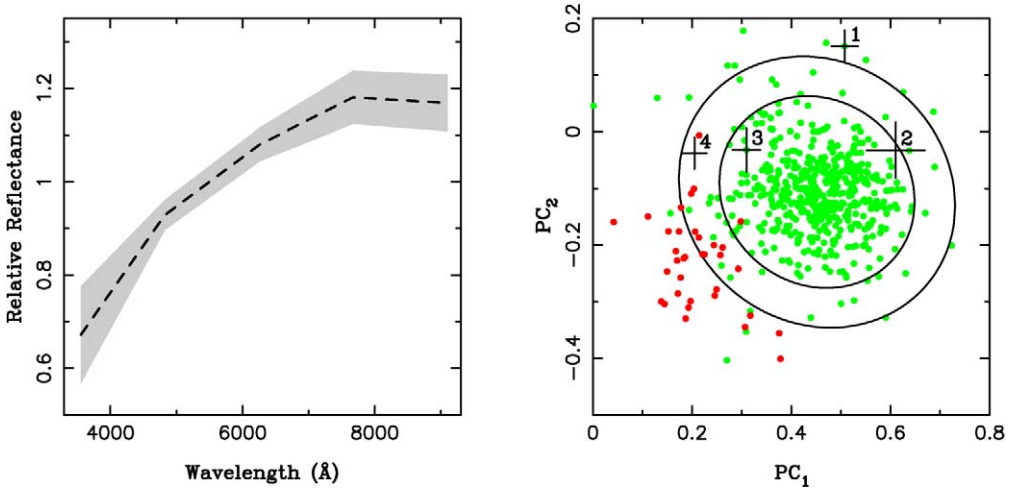

Fig. 23. Left: Dashed curve shows a mean 5-color spectrum for 499 small Eos members from the SDSS database (release 3.0; see Jurić et al., 2002, and http://www.astro.princeton.edu/~ivezic/sdssmoc/sdssmoc.html) whose principal spectral components have an error smaller than 0.1 (here we normalized the result to unity at 550 nm as conventional). The shaded zone shows a standard deviation interval about the mean. Right: The Eos family members (light symbols) projected onto the plane of spectral principal components PC_1 and PC_2 (e.g., Nesvorný et al., 2005a); here we use again the sample of 499 asteroids observed with SDSS with small enough errors. The two ellipses show a 90% (inner ellipse), resp. 99% (outer ellipse), confidence level of a formal relation between the two components that define the Eos family as a cluster of data in these variables. Objects outside these limits are likely alien to the family. Here we list large members in this zone: (i) 1—(8340) Mumma, (ii) 2—(1755) Lorbach, (iii) 3—(4843) Megantic, and (iv) 4—(4431) Holeungholee; the horizontal and vertical intervals show error-bars of the data. The last two were classified X-types by the narrow-band spectroscopy, while (8340) Mumma received D classification and (1755) Lorbach T classification (see Fig. 21). For sake of comparison we also show the neighboring Veritas family (dark symbols), classified as C-type group.

al., 2004; Mothé-Diniz et al., 2005). They are shifted out of the center of the Eos group toward smaller PC_1 values; this indicates they have a flatter spectrum than other objects. These objects are likely interlopers.

The other two are (8340) Mumma, denoted 1, and (1755) Lorbach, denoted 2. They are particularly interesting because our analysis of their narrow-band photometry (Section 4.1) classified them as D and T, respectively. These classes are generally compatible with the family (Section 2.2) but they could also be interlopers. For (8340) Mumma, SDSS photometry places it toward the D group (high PC_2 value). In fact its displacement in PC_2 component, relative to the family center, is larger than other D-type Eos members, such that (8340) Mumma occurs beyond the 99% confidence level of the family PC_1–PC_2 identification. Thus, SDSS data suggests that (8340) Mumma is an interloper, in spite its D-type classification. The same analysis rejects (1755) Lorbach as an Eos member in spite of its T-type classification because this asteroid resides at the 90% confidence level line for being associated with the Eos family.

Finding these last two asteroids incompatible with membership to the Eos family is "good news" since their respective values of the C parameter ($C = -2.1 \times 10^{-4}$ AU for (8340) Mumma; $C = 5.1 \times 10^{-4}$ AU for (1755) Lorbach) are far too large to explain them using our Yarkovsky diffusion model (e.g., Figs. 12, 14, and 22).

5. Conclusions

In this paper, we have attempted to understanding the structure and history of the Eos asteroid family. Using our Yarkovsky diffusion model, we were able to match several outstanding features seen in the proper element space (e.g., the sharp termination of the family at the J7/3 MMR; the migration of asteroids along the z_1 secular resonance). Our model also predicted the relative fraction of Eos family members on both sides of the J9/4 MMR and it can be used to understand the concentration of small asteroids at extreme semimajor axis values (see also Vokrouhlický et al., 2005). Moreover, by matching the semimajor axis distribution of Eos family members, we were able to estimate that the family is $T = 1.3$ Gyr old, some 30% younger than used by Nesvorný et al. (2005a). Interestingly, this brings the Eos "data point" closer to the empirical relation between the average spectral slope PC_1 within the family and its age determined by these authors (see Fig. 11 in Nesvorný et al., 2005a).

The mineralogy of the Eos parent body is still a puzzle (e.g., Burbine et al., 2001; Mothé-Diniz and Carvano, 2005). For this reason, caution should be used when interpreting the spectra of Eos family members. Nevertheless, we predict that the majority of small asteroids inside the z_1 stream are most likely from the Eos family. Similarly, we ruled out several asteroids as interlopers based on their orbital position, which was inconsistent with Yarkovsky evolution, and their spectral features/taxonomic type (e.g., (8340) Mumma and (1755) Lorbach).

Despite our successes, we cannot yet fully reproduce the large eccentricity and, especially, inclination dispersion of the Eos family (Section 1). We believe this problem may have been produced by a projectile striking the Eos parent body from the out-of-plane direction. Bottke et al. (1994) analyzed the impact velocity distribution for main-belt projectiles on a putative Eos family progenitor and found that asteroids are a factor $\simeq$4 more likely to strike from the out-of-plane than in-plane direction. This feature could produce an anisotropic ejecta velocity field, with the highest-velocity fragments having the same trajectory as the projectile. Given the probabilities above, this could produce a larger dispersion of inclinations (and eccentricities) than one might expect.

To examine this issue more closely, we note that our best-fit solution from Section 3.2 indicates that $D \simeq 4$ km asteroids, which dominate the observed Eos population, were ejected with an along-track velocity component of $\simeq$100 m/s (we investigated only the semimajor axis dispersion). If this value were applied used to the other two components, radial and normal, we would expect maximum eccentricity and inclination dispersions of $\simeq$0.024 and $\simeq$0.012. The observed dispersion, however, is $\simeq$0.040 and $\simeq$0.025, larger than the maximum estimated values. By accounting for the larger characteristic velocities of ejecta in the normal and radial directions as explained above, we believe we can explain this mismatch.[8]

Other than the Koronis family (Bottke et al., 2001), the Eos family is the second main-belt family to have received a thorough analysis using the modern dynamical tools. By studying other families, we hope—among other goals—to constrain their ages enough to decipher the overall history of the main belt.

Acknowledgments

This work, David Vokrouhlický and Miroslav Brož, has been supported by the Grant Agency of the Czech Republic, Grant 205/05/2737. Research funds for William Bottke and David Nesvorný were provided by NASA's Planetary Geology and Geophysics Program. The work of Daniela Lazzaro has been supported by CNPq through Grant No. 306605/2003-1. We thank Andrea Milani and Zoran Knežević for providing us with their numerically computed secular proper frequencies across the whole asteroid belt and a related software allowing to display location of various high-order secular resonances. We also thank Hal Levison for the suggestion to study the role of faint young Sun (Section 3.2) and Zeljko Ivezić for providing us with the SDSS moving objects catalogue (Data release 3.0). Reviews by Valerio Carruba and Alberto Cellino were much helpful to prepare the final version of the paper. Observations obtained at the Hale Telescope, Palomar Observatory are part of a collaboration between the California Institute of Technology, NASA/JPL, and Cornell University.

[8] The same feature is seen in the young Veritas family (e.g., Nesvorný et al., 2003), whose initial velocity field holds a high degree of anisotropy. For instance, from the relative measure of the inclination and semimajor axis dispersion of Veritas multi-kilometer members we determine that the ratio of the mean normal vs transverse velocity components was 3–5 in this case. It is tempting to assume a similar explanation as for the Eos.

References

Bahcall, J.N., Pinsonneault, M.H., Basu, S., 2001. Solar models: Current epoch and time dependences, neutrinos, and helioseismological properties. Astrophys. J. 555, 990–1012.

Bell, J.F., 1989. Mineralogical clues to the origin of asteroid dynamical families. Icarus 78, 426–440.

Bell, J.F., Hawke, B.R., Owensby, P.D., 1987. Carbonaceous chondrites from S-type asteroids? Bull. Am. Astron. Soc. 19, 841.

Bendjoya, P., Zappalà, V., 2002. Asteroid family identification. In: Bottke, W.F., Cellino, A., Paolicchi, P., Binzel, R.P. (Eds.), Asteroids III. Univ. of Arizona Press, Tucson, pp. 613–618.

Benz, W., Asphaug, E., 1999. Catastrophic disruptions revisited. Icarus 142, 5–20.

Bertotti, B., Farinella, P., Vokrouhlický, D., 2003. Physics of the Solar System. Kluwer Academic, Dordrecht.

Binzel, R.P., 1988. Collisional evolution in the Eos and Koronis asteroid families: Observational and numerical results. Icarus 73, 303–313.

Binzel, R.P., Rivkin, A.S., Stuart, J.S., Harris, A.W., Bus, S.J., Burbine, T.H., 2004. Observed spectral properties of near-Earth objects: Results for population distribution, source regions, and space weathering processes. Icarus 170, 259–294.

Bottke, W.F., Nolan, M.C., Greenberg, R., Kolvoord, R.A., 1994. Velocity distributions among colliding asteroids. Icarus 107, 255–268.

Bottke, W.F., Rubincam, D.P., Burns, J.A., 2000. Dynamical evolution of main belt meteoroids: Numerical simulations incorporating planetary perturbations and Yarkovsky thermal forces. Icarus 145, 301–331.

Bottke, W.F., Vokrouhlický, D., Brož, M., Nesvorný, D., Morbidelli, A., 2001. Dynamical spreading of asteroid families via the Yarkovsky effect: The Koronis family and beyond. Science 294, 1693–1695.

Bottke, W.F., Vokrouhlický, D., Rubincam, D.P., Brož, M., 2002. Dynamical evolution of asteroids and meteoroids using the Yarkovsky effect. In: Bottke, W.F., Cellino, A., Paolicchi, P., Binzel, R.P. (Eds.), Asteroids III. Univ. of Arizona Press, Tucson, pp. 395–408.

Bottke, W.F., Durda, D.D., Nesvorný, D., Jedicke, R., Morbidelli, A., Vokrouhlický, D., Levison, H.F., 2005a. The fossilized size distribution of the main asteroid belt. Icarus 175, 111–140.

Bottke, W.F., Durda, D.D., Nesvorný, D., Jedicke, R., Morbidelli, A., Vokrouhlický, D., Levison, H.F., 2005b. Linking the collisional history of the main asteroid belt to its dynamical excitation and depletion. Icarus 179, 63–94.

Bottke, W.F., Durda, D.D., Nesvorný, D., Jedicke, R., Morbidelli, A., Vokrouhlický, D., Levison, H.F., 2005c. The origin and evolution of stony meteorites. In: Knežević, Z., Milani, A. (Eds.), Dynamics of Populations of Planetary Systems. Cambridge Univ. Press, Cambridge, pp. 357–376.

Brouwer, D., 1951. Secular variations of the orbital elements of minor planets. Astron. J. 56, 9–32.

Brown, E.W., 1932. Observation and gravitational theory in the Solar System. Publ. Astron. Soc. Pacific 44, 21–40.

Brož, M., Vokrouhlický, D., Roig, F., Nesvorný, D., Bottke, W.F., Morbidelli, A., 2005. Yarkovsky origin of the unstable asteroids in the 2/1 mean motion resonance with Jupiter. Mon. Not. R. Astron. Soc. 359, 1437–1455.

Burbine, T.H., Binzel, R.P., Bus, S.J., Clark, B.E., 2001. K asteroids and CO3/CV3 chondrites. Meteorit. Planet. Sci. 36, 245–253.

Bus, S.J., Binzel, R.P., 2002a. Phase II of the small main-belt asteroid spectroscopic survey. The observations. Icarus 158, 106–145.

Bus, S.J., Binzel, R.P., 2002b. Phase II of the small main-belt asteroid spectroscopic survey. A feature-based taxonomy. Icarus 158, 146–177.

Campo Bagatin, A., Petit, J.-M., 2001. Effects of the geometric constraints on the size distributions of debris in asteroidal fragmentation. Icarus 149, 210–221.

Čapek, D., Vokrouhlický, D., 2004. The YORP effect with finite thermal conductivity. Icarus 172, 526–536.

Carpino, M., Gonczi, R., Farinella, P., Froeschlé, Ch., Froeschlé, C., Paolicchi, P., Zappalà, V., 1986. The accuracy of proper orbital elements and the properties of asteroid families: Comparison with the linear theory. Icarus 68, 55–76.

Carruba, V., Burns, J.A., Bottke, W.F., Nesvorný, D., 2003. Orbital evolution of the Gefion and Adeona asteroid families: Close encounters with massive asteroids and the Yarkovsky effect. Icarus 162, 308–327.

Carruba, V., Michtchenko, T.A., Roig, F., Ferraz-Mello, S., Nesvorný, D., 2005. On the V-type asteroids outside the Vesta family. I. Interplay of nonlinear secular resonances and the Yarkovsky effect: The cases of 956 Elisa and 809 Lundia. Astron. Astrophys. 441, 819–830.

Cellino, A., Michel, P., Tanga, P., Zappalà, V., Paolicchi, P., Dell'Oro, A., 1999. The velocity–size relationship for members of asteroid families and implications for the physics of catastrophic collisions. Icarus 141, 79–95.

Cellino, A., Bus, S.J., Doressoundiram, A., Lazzaro, D., 2002. Spectroscopic properties of asteroid families. In: Bottke, W.F., Cellino, A., Paolicchi, P., Binzel, R.P. (Eds.), Asteroids III. Univ. of Arizona Press, Tucson, pp. 633–643.

Davis, D.R., Farinella, P., Paolicchi, P., Weidenschilling, S.J., Binzel, R.P., 1989. Asteroid collisional history: Effects on sizes and spins. In: Binzel, R.P., Gehrels, T., Matthews, M.S. (Eds.), Asteroids II. Univ. of Arizona Press, Tucson, pp. 805–826.

Dell'Oro, A., Bigongiari, G., Paolicchi, P., Cellino, A., 2004. Asteroid families: Evidence of aging of the proper elements. Icarus 169, 341–356.

Dermott, S.F., Grogan, K., Durda, D.D., Jayaraman, S., Kehoe, T.J.J., Kortenkamp, S.J., Wyatt, M.C., 2001. Orbital evolution of interplanetary dust. In: Grün, E., Gustafson, B.A.S., Dermott, S.F., Fechtig, H. (Eds.), Interplanetary Dust. Springer, Berlin, pp. 569–639.

Dohnanyi, J.W., 1969. Collisional models of asteroids and their debris. J. Geophys. Res. 74, 2531–2554.

Doressoundiram, A., Barucci, M.A., Fulchignoni, M., Florczak, M., 1998. Eos family: A spectroscopic study. Icarus 131, 15–31.

Farinella, P., Vokrouhlický, D., 1999. Semimajor axis mobility of asteroidal fragments. Science 283, 1507–1510.

Farinella, P., Carpino, M., Froeschlé, Ch., Froeschlé, C., Gonczi, R., Knežević, Z., Zappalà, V., 1989. The ages of asteroid families. Astron. Astrophys. 217, 298–306.

Farinella, P., Vokrouhlický, D., Hartmann, W.K., 1998. Meteorite delivery via Yarkovsky orbital drift. Icarus 132, 378–387.

Fujiwara, A., 1982. Complete fragmentation of the parent bodies of Themis, Eos, and Koronis families. Icarus 52, 434–443.

Fukugita, M., Ichikawa, T., Gunn, J.E., Doi, M., Shimasaku, K., Schneider, D.P., 1996. The Sloan Digital Sky Survey photometric system. Astron. J. 111, 1748–1756.

Hardorp, J., 1978. The Sun among the stars. Astron. Astrophys. 63, 383–390.

Hirayama, K., 1918. Groups of asteroids probably of common origin. Astron. J. 31, 185–188.

Ivezić, Z., and 32 colleagues, 2001. Solar System objects observed in the Sloan Digital Sky Survey commissioning data. Astron. J. 122, 2749–2784.

Ivezić, Z., Lupton, R.H., Jurić, M., Tabachnik, S., Quinn, T., Gunn, J.E., Knapp, G.R., Rockosi, C.M., Brinkmann, J., 2002. Color confirmation of asteroid families. Astron. J. 124, 2943–2948.

Jedicke, R., Nesvorný, D., Whiteley, R., Ivezić, Z., Jurić, M., 2004. An age–color relationship for main-belt S-complex asteroids. Nature 429, 275–277.

Jurić, M., and 12 colleagues, 2002. Comparison of positions and magnitudes of asteroids observed in the Sloan Digital Sky Survey with those predicted for known asteroids. Astron. J. 124, 1776–1787.

Knežević, Z., Milani, A., 2000. Synthetic proper elements for outer main belt asteroids. Celest. Mech. Dynam. Astron. 78, 17–46.

Knežević, Z., Milani, A., 2003. Proper element catalogs and asteroid families. Astron. Astrophys. 403, 1165–1173.

Lazzaro, D., Angelia, C.A., Carvanoa, J.M., Mothé-Diniz, T., Duffard, R., Florczak, M., 2004. S^3OS^2: The visible spectroscopic survey of 820 asteroids. Icarus 172, 179–220.

Levison, H., Duncan, M., 1994. The long-term dynamical behavior of short-period comets. Icarus 108, 18–36.

Love, S.G., Ahrens, T.J., 1996. Catastrophic impacts on gravity dominated asteroids. Icarus 124, 141–155.

Marzari, F., Davis, D.R., Vanzani, V., 1995. Collisional evolution of asteroid families. Icarus 113, 168–187.

Migliorini, F., Zappalà, V., Vio, R., Cellino, A., 1995. Interlopers within asteroid families. Icarus 118, 271–291.

Milani, A., Farinella, P., 1994. The age of Veritas asteroid family deduced by chaotic chronology. Nature 370, 40–42.

Milani, A., Farinella, P., 1995. An asteroid on the brink. Icarus 115, 209–212.

Milani, A., Knežević, Z., 1990. Secular perturbation theory and computation of asteroid proper elements. Celest. Mech. Dynam. Astron. 49, 347–411.

Milani, A., Knežević, Z., 1992. Asteroid proper elements and secular resonances. Icarus 98, 211–232.

Milani, A., Knežević, Z., 1994. Asteroid proper elements and the dynamical structure of the asteroid main belt. Icarus 107, 219–254.

Michel, P., Benz, W., Tanga, P., Richardson, D.C., 2001. Collisions and gravitational reaccumulation: Forming asteroid families and satellites. Science 294, 1696–1700.

Michel, P., Tanga, P., Benz, W., Richardson, D.C., 2002. Formation of asteroid families by catastrophic disruption: Simulations with fragmentation and gravitational reaccumulation. Icarus 160, 10–23.

Mothé-Diniz, T., Carvano, J.M., 2005. 221 Eos: A remnant of a partially differentiated parent body? Astron. Astrophys. 442, 727–729.

Mothé-Diniz, T., Roig, F., Carvano, J.M., 2005. Reanalysis of asteroid families structure through visible spectroscopy. Icarus 174, 54–80.

Moons, M., Morbidelli, A., Migliorini, F., 1998. Dynamical structure of the 2/1 commensurability with Jupiter and the origin of the resonant asteroids. Icarus 135, 458–468.

Morbidelli, A., 2002. Modern Celestial Mechanics: Aspects of Solar System Dynamics. Taylor & Francis, London.

Morbidelli, A., Nesvorný, D., 1999. Numerous weak resonances drive asteroids toward terrestrial planets orbits. Icarus 139, 295–308.

Morbidelli, A., Vokrouhlický, D., 2003. The Yarkovsky-driven origin of near-Earth asteroids. Icarus 163, 120–134.

Morbidelli, A., Zappalà, V., Moons, M., Cellino, A., Gonczi, R., 1995. Asteroid families close to mean motion resonances: Dynamical effects and physical implications. Icarus 118, 132–154.

Morbidelli, A., Nesvorný, D., Bottke, W.F., Michel, P., Vokrouhlický, D., Tanga, P., 2003. The shallow magnitude distribution of asteroid families. Icarus 162, 328–336.

Nesvorný, D., Bottke, W.F., 2004. Detection of the Yarkovsky effect for main belt asteroids. Icarus 170, 324–342.

Nesvorný, D., Morbidelli, A., 1998. Three-body mean motion resonances and the chaotic structure of the asteroid belt. Astron. J. 116, 3029–3037.

Nesvorný, D., Morbidelli, A., Vokrouhlický, D., Bottke, W.F., Brož, M., 2002a. The Flora family: A case of the dynamically dispersed collisional swarm? Icarus 157, 155–172.

Nesvorný, D., Bottke, W.F., Dones, L., Levison, H.F., 2002b. The recent breakup of an asteroid in the main-belt region. Nature 417, 720–722.

Nesvorný, D., Bottke, W.F., Levison, H.F., Dones, L., 2003. Recent origin of the Solar System dust bands. Astrophys. J. 591, 486–497.

Nesvorný, D., Jedicke, R., Whiteley, R.J., Ivezić, Ž., 2005a. Evidence for asteroid space weathering from the Sloan Digital Sky Survey. Icarus 173, 132–152.

Nesvorný, D., Vokrouhlický, D., Bottke, W.F., Sykes, M.V., 2005b. Properties of asteroid dust bands and their sources. Icarus. In press.

Nesvorný, D., Enke, B.L., Bottke, W.F., Durda, D.D., Asphaug, E., Richardson, D.C., 2005c. Karin cluster formation via asteroid impact. Icarus. Submitted for publication.

O'Brien, D.P., Greenberg, R., 2003. Steady-state size distributions for collisional populations: Analytical solution with size-dependent strength. Icarus 164, 334–345.

Paolicchi, P., Verlicchi, A., Cellino, A., 1996. An improved semi-empirical model of catastrophic impact processes. I. Theory and laboratory experiments. Icarus 121, 126–157.

Petit, J.-M., Farinella, P., 1993. Modeling the outcomes of high-velocity impacts between small Solar System bodies. Celest. Mech. Dynam. Astron. 57, 1–28.

Press, W.H., Teukolsky, S.A., Vetterlink, W.T., Flannery, B.P., 1999. Numerical Recipes in Fortran 77. Cambridge Univ. Press, Cambridge.

Quinn, T.R., Tremaine, S., Duncan, M., 1991. A three million year integration of the Earth's orbit. Astron. J. 101, 2287–2305.

Rubincam, D.P., 2000. Radiative spin-up and spin-down of small asteroids. Icarus 148, 2–11.

Ryan, E.V., Melosh, H.J., 1998. Impact fragmentation: From the laboratory to asteroids. Icarus 133, 1–24.

Šidlichovský, M., Nesvorný, D., 1997. Frequency modified Fourier transform and its applications to asteroids. Celest. Mech. Dynam. Astron. 65, 137–148.

Stokes, G.H., Evans, J.B., Larson, S.M., 2002. Near-Earth asteroid search programs. In: Bottke, W.F., Cellino, A., Paolicchi, P., Binzel, R.P. (Eds.), Asteroids III. Univ. of Arizona Press, Tucson, pp. 45–54.

Tanga, P., Cellino, A., Michel, P., Zappalà, V., Paolicchi, P., Dell'Oro, A., 1999. On the size distribution of asteroid families: The role of geometry. Icarus 141, 65–78.

Tedesco, E.F., Noah, P.V., Noah, M., Price, S.D., 2002. The supplemental IRAS minor planet survey. Astron. J. 123, 1056–1085.

Tholen, D.J., 1989. Asteroid taxonomic classifications. In: Binzel, R.P., Gehrels, T., Matthews, M.S. (Eds.), Asteroids II. Univ. of Arizona Press, Tucson, pp. 1139–1150.

Tody, D., 1986. The IRAF data reduction and analysis system. In: Drawford, D.L. (Ed.), Instrumentation in Astronomy VI. Society of Photo-Optical Instrumentation Engineers, Bellingham, p. 733.

Tsiganis, K., Varvoglis, H., Morbidelli, A., 2003. Short-lived asteroids in the 7/3 Kirkwood gap and their relationship to the Koronis and Eos families. Icarus 166, 131–140.

Tüg, H., 1977. Vertical extinction on La Silla. Messenger 11, 7–8.

Veeder, G.J., Matson, D.L., Owensby, P.D., Gradie, J.C., Bell, J.F., Tedesco, E.F., 1995. Eos, Koronis, and Maria family asteroids: Infrared (JHK) photometry. Icarus 114, 186–196.

Vokrouhlický, D., 1998. Diurnal Yarkovsky effect as a source of mobility of meter-sized asteroidal fragments. I. Linear theory. Astron. Astrophys. 335, 1093–1100.

Vokrouhlický, D., 1999. A complete linear model for the Yarkovsky thermal force on spherical asteroid fragments. Astron. Astrophys. 344, 362–366.

Vokrouhlický, D., Brož, M., 2002. Interaction of the Yarkovsky-drifting orbits with weak resonances: Numerical evidence and challenges. In: Celletti, A., Ferraz-Mello, S., Henrard, J. (Eds.), Modern Celestial Mechanics: From Theory to Applications. Kluwer Academic, Dordrecht, pp. 467–472.

Vokrouhlický, D., Čapek, D., 2002. YORP-induced long-term evolution of the spin state of small asteroids and meteoroids. Rubincam's approximation. Icarus 159, 449–467.

Vokrouhlický, D., Farinella, P., 1999. The Yarkovsky seasonal effect on asteroidal fragments: A nonlinearized theory for spherical bodies. Astron. J. 118, 3049–3060.

Vokrouhlický, D., Nesvorný, D., Bottke, W.F., 2003. Thermal torques produce spin vector alignments among Koronis family asteroids. Nature 425, 147–151.

Vokrouhlický, D., Brož, M., Bottke, W.F., Nesvorný, D., Morbidelli, A., 2005. Yarkovsky chronology of young asteroid families. Icarus. In press.

Xu, S., Binzel, R.P., Burbine, T.H., Bus, S.J., 1995. Small main-belt asteroid spectroscopic survey: Initial results. Icarus 115, 1–35.

Zappalà, V., Farinella, P., Knežević, Z., Paolicchi, P., 1984. Collisional origin of the asteroid families: Mass and velocity distributions. Icarus 59, 261–285.

Zappalà, V., Cellino, A., Farinella, P., Knežević, Z., 1990. Asteroid families. I. Identification by hierarchical clustering and reliability assessment. Astron. J. 100, 2030–2046.

Zappalà, V., Bendjoya, P., Cellino, A., Farinella, P., Froeschlé, C., 1995. Asteroid families: Search of a 12,487-asteroid sample using two different clustering techniques. Icarus 116, 291–314.

Zappalà, V., Cellino, A., Dell'Oro, A., Migliorini, F., Paolicchi, P., 1996. Reconstructing the original velocity fields of asteroid families. Icarus 124, 156–180.

Zappalà, V., Bendjoya, P., Cellino, A., Di Martino, M., Doressoundiram, A., Manara, A., Migliorini, F., 2000. Fugitives from the Eos family: First spectroscopic confirmation. Icarus 145, 4–11.

Zellner, B., Tholen, D.J., Tedesco, E.F., 1985. The eight-color asteroid survey: Results for 589 minor planets. Icarus 61, 355–416.